Polygon-Informed Cross-Track Altimetry (PICTA) derived river level profiles for the Bengal Tiger habitats in Nepal

Author:
G.D. (Bart) van den Broek
4919157

Thesis Committee:
Dr.ir. D.C. (Cornelis) Slobbe
Prof. Dr. T.A. (Thom) Bogaard
Msc. F. (Frithjof) Ehlers

Master Thesis
Geoscience and Remote Sensing
Delft University of Technology
The Netherlands
August 2024

Abstract

The Karnali River in Bardia National Park (BNP), Nepal, is crucial for sustaining the habitats of endangered Bengal Tigers. However, gathering data to analyze this remote river's behavior presents significant challenges due to the remote and mountainous terrain of BNP. This thesis explores an approach using the altimetry satellite Sentinel-6 to measure river water surface elevations (WSEs), specifically utilizing the innovative Polygon-Informed Cross-Track Altimetry (PICTA) method. By integrating fully-focused Synthetic Aperture Radar (FF-SAR) data from Sentinel-6 with a static river polygon, we aimed to retrack WSEs and unlock new insights into the Karnali River's dynamics.

The objective of this thesis was to evaluate the performance and potential of the PICTA method in deriving precise river level profiles for the Karnali River. The research questions addressed include: How does PICTA compare to in-situ water surface height measurements? How well does it align with the SWOT mission, which also measures river water levels? How do river level profiles change over time? And how does the use of a static river polygon influence water level uncertainty for the dynamic Karnali River?

The PICTA method successfully derived water surface elevations for a 10-kilometer-long section of the Karnali River. Over a year-long period from February 2023 to February 2024, we generated 38 detailed PICTA river level profiles. These profiles revealed the relationship between measured WSE fluctuations, river slope, and river width over time. We observed that both WSE fluctuations and river slope decreased at sections where the Karnali River could overflow its banks during high water. Notable gaps in the profiles, such as transitions from a single channel to a multichannel system, provided insights into the interaction between river characteristics and the PICTA algorithm.

The PICTA-derived WSE time series closely matched in-situ measurements at the river gauge station at Chisapani, Nepal, showing similar seasonal trends and peak differences. When comparing PICTA and SWOT profiles, we observed a mean bias near zero and a scaled MAD of approximately 20 cm. Dynamic river polygons based on SWOT data further improved the agreement, reducing the scaled MAD by 10 cm and increasing retracked PICTA data points. Using a static river polygon introduced WSE uncertainties ranging from 5 cm in the summer to 20 cm in the winter, averaging 10 cm over time. This study suggests that dynamic polygons could enhance the accuracy of PICTA derived WSEs.

Ultimately, PICTA's ability to capture and relate seasonal trends to local hydraulic behavior underscores its significant potential. This research advances our understanding of the Karnali River's dynamics and demonstrates PICTA's ability to derive river water levels in a remote, mountainous region. These insights could constribute to support better conservation efforts for BNP's vital Bengal Tiger habitats.

Contents

1 Introduction

1.1 Background

BNP in western Nepal (Fig. 1) serves as a critical habitat for the Bengal Tiger [29]. The species are globally recognized as endangered due to the threats of climate change and human interference [35]. As human population grows, the amount of wild habitat for the tigers decreases. However, the tiger population in BNP has been successful [29]. This is evidenced by the remarkable increase of the tiger population, which more than doubled from 2012 to 2022 [23]. This growth is mainly due to the balanced ecosystem in the area. The grasslands in BNP are essential for the tigers as they attract their prey. The growth potential of grasses and the grassland dynamics depend on the hydrological conditions in the area. Especially the hydraulic behaviour of the rivers in the area impacts the long-term behaviour of the ecosystem [7].

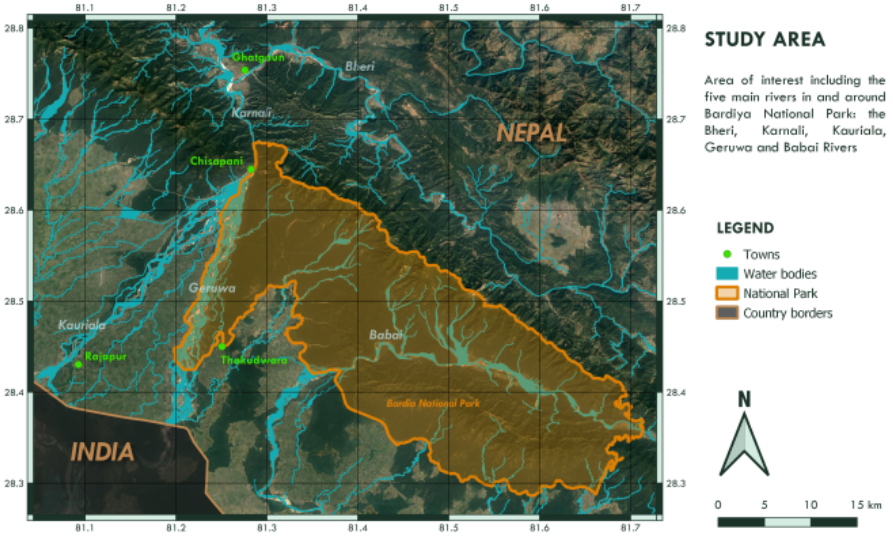

Figure 1: Map from [11] of BNP including Bheri, Karnali, Kauriala, Geruwa and Babai Rivers in West-Nepal.

The BNP's prosperity is inextricably linked to two major rivers: the Babai and the Karnali. The Babai flows from the east through the heart of BNP. The Karnali is a vital water source commencing from the Tibetan Plateau, meandering through the Himalayas, and passing the BNP in the north-west. As The Karnali River exits the mountainous region at Chisapani, it divides into the Kauriala and Geruwa Rivers. This divergence marks the beginning of a unique braided river system that significantly influences the park's diverse landscapes, which include forests, shrublands, grasslands, aquatic ecosystems, and agricultural areas [37]. The Geruwa River in the west of BNP plays an important role for the area. It acts as a natural demarcation for BNP and provides a life-sustaining boundary alongside the Rajapur agricultural zone. This river, along with the Kauriala, rejoins post the Indian border to form the Karnali again, eventually contributing to the Ganges River system. The Bheri river is the main tributary contributing to the Karnali river flow. Understanding the variability in water levels of these rivers is crucial for grasping their hydraulic behavior [7]. This can offer vital insights for ongoing research into sustainable habitat management for the Bengal Tiger.

This study will focus on the Karnali River, one of the main rivers flowing into BNP. The behavior and characteristics of the Karnali River, including its bifurcation with the Bheri River, are of great interest to hydrologists. Previous research has analyzed the climate and discharge patterns around the Karnali River Basin (KRB) [26].The climate in the KRB is mainly influenced by the monsoonal system, physiography of the region, and westerlies. The monsoon which originates from the Indian Ocean and the westerlies play active roles to bring precipitation into the region. During the summer monsoon season (June to September) KRB receives approximately 80% of the annual precipitation of 1530 mm. The average monthly precipitation of KRB from 1981 to 2012 is shown in Fig. 2. The distribution of the monthly average rainfall in the KRB shows that highest precipitation occurs in July (377 mm) and lowest in November (10 mm). In the KRB the precipitation amount peaks in the months of July and August.

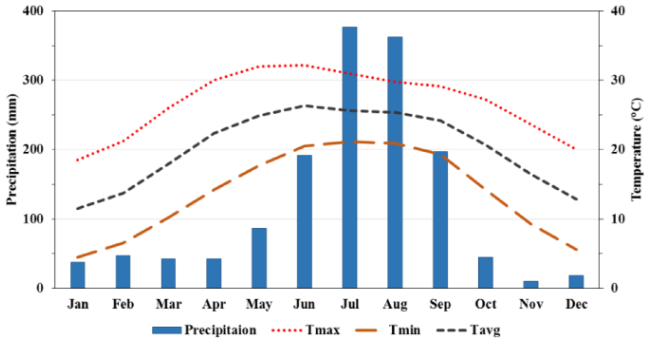

Figure 2: Average monthly precipitation and temperature (minimum, maximum, and average) in the KRB from 1981 to 2012 [26].

The average annual discharge at the KRB's Chisapani outlet is measured at 1369 m^3/s, with the highest monthly runoff in August (4278 m^3/s) and the lowest in February (302 m^3/s), as depicted in Fig. 3. There is a positive correlation between monthly river discharge and precipitation within the KRB, with peak discharges typically occurring one month after the highest rainfall. This delay might be attributed to the basin's extensive size, which can prolong the time it takes for rainwater to travel as surface and subsurface runoff to the outlet, or it could suggest that snow and glacial melt in the region significantly influence the discharge characteristics [26]. Furthermore, river discharge in the KRB appears to be particularly responsive to changes in pre-monsoon temperatures. Discharge starts to rise in May, reaching its peak in August, coinciding with the onset of higher temperatures that contribute to snow and glacier melt, thus enhancing stream flow. This increased runoff persists through the monsoon and into the post-monsoon period when temperatures remain elevated. Notably, after August, the discharge at Chisapani often exceeds the precipitation levels in the KRB, likely due to substantial contributions from groundwater and glacial melt [26].

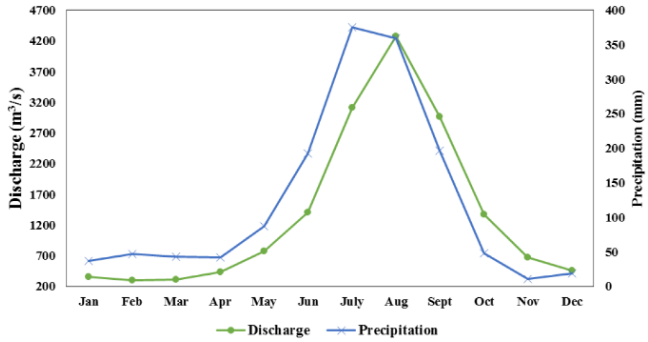

Figure 3: Monthly average precipitation and discharge relation in KRB, during 1981-2010 [26].

Analyzing the KRB using in-situ data presents significant challenges due to the acute problem of lacking a good network of stations [26]. Only the Chisapani river gauge station at the Karnali River provides historical water level data. A network of stations is necessary to assess changes in river water levels throughout the region [4]. But despite growing challenges for water resource management across the entire globe, the availability of in-situ river monitoring data is decreasing [36][27].

Altimetry satellites can offer solutions [27]. With the help of satellite altimeters we can measure the round trip distance to a target, and infer from that the water surface elevation (WSE) using knowledge about the orbit and geophysical corrections [34]. Satellite radar altimetry has demonstrated its worth as an essential tool for gathering data on water levels in rivers and lakes, particularly in areas with limited gauging stations [28][36] [33]. Providing consistent and worldwide information about water levels, it operates independently of local infrastructure or political factors, significantly enhancing the efficiency and cost-effectiveness of collecting hydrological data.

1.2 Previous Work

Satellite radar altimeters are primarily nadir-looking instruments [34], meaning they measure the water surface elevation (WSE) at the intersection points between the satellite ground track and a river, known as virtual stations [8]. These virtual stations function like river gauges, with a temporal resolution of 10 days for Sentinel-6 [17]. Consequently, most missions provide virtual station time series of water levels at locations where their

repeat orbits cross the river [36]. This is also the case for BNP, where multiple virtual stations are distributed throughout the region. The development of un-focused Synthetic Aperture Radar (UF-SAR) processed altimetry has significantly improved the along-track footprint size to approximately 300 meters. This advancement has been utilized by missions such as CryoSAT-2, Sentinel-3, and Sentinel-6 to enhance the measurements and analysis of rivers. [15]. The improved UF-SAR resolution allows for increased number of WSE measurements, enabling the creation of altimetry point profiles at river crossings [30].

1.3 Motivation

More recently, FF-SAR processed altimetry has been introduced, leveraging Sentinel-6 to improve along-track resolution to 0.5-1 m. With FF-SAR, the river signal is clearly visible not only near the ground track (nadir), which is used in the virtual stations method, but also for cross-track locations within a ground swath of approximately 14 km width [15]. PICTA utilizes FF-SAR data in combination with a river polygon to derive WSEs for rivers located cross-track [2]. This method has been used to construct WSE river profiles of several kilometers in length. While PICTA has so far only been applied to river measurements in France [2], applying the method to measure the Karnali River in the diverse topographical region of BNP could reveal its broader utility and provide new insights into the method's performance.

We can assess the performance of PICTA for the Karnali River by comparing the WSE with other measurement techniques. First, we can compare PICTA with data from a local in-situ river gauge station, which provides long-term water surface height data. Second, we can compare PICTA with measurements from the Surface Water and Ocean Topography (SWOT) mission [3], which offers high-resolution river measurements globally. Additionally, we can evaluate the potential uncertainty in PICTA derived WSEs due to the use of a static river polygon [2], which may not accurately capture the dynamic nature of the Karnali River, particularly given its significant seasonal variations [26]. The motivation behind this study is to assess the performance of PICTA and its potential to provide insights into the hydraulic behavior of the Karnali River. These insights can contribute to a better understanding of the BNP region and the habitat of the Bengal Tigers.

1.4 Research Objectives

This study utilized the PICTA method to assess the following research objectives:

- *To assess the quality of PICTA derived river level profiles for the Karnali River in BNP.*
- *To assess the potential of PICTA derived river level profiles to provide insights into the hydraulic behavior of the Karnali River in BNP.*

To fulfil the research objectives, the following research questions will be investigated and answered for the Karnali river in mountainous region of BNP:

- *What is the agreement between PICTA and in-situ derived water surface height time series?*
- *What is the agreement between PICTA and SWOT derived river level profiles?*
- *How do the river level profiles vary over time?*
- *How does river water level uncertainty vary over time using a static river polygon?*

1.5 Outline

This thesis is organized into five main chapters. In the second section, **FF-SAR Altimetry**, we introduce the concept of FF-SAR, discussing its fundamental principles and the processing steps involved. The third section, **Data and Methods**, details the data selection process, covering Sentinel-6 data, river polygon and centerline data, SWOT data, and in-situ data. It also elaborates on the methods for retrieving river level profiles, including measurement principles and retracking. This is followed by descriptions of the analysis methods for the retracked river water levels, structured around the four research questions. The fourth section, **Results and Discussion**, presents and discusses the results for each research question, including comparisons between FF-SAR and in-situ water level time series, analysis of PICTA and SWOT river level profiles, and the assessment of river level profiles over time, along with an uncertainty assessment over time. The fifth section, **Conclusion**, summarizes the insights gained from FF-SAR-derived river level profiles by answering the research questions and provides recommendations for future research.

2 FF-SAR altimetry

In this section, we first introduce the concept and theory of FF-SAR processing altimetry, highlighting its advantages. This is followed by a study of the processing steps involved to obtain FF-SAR data, which will be utilized to retrack river water levels.

2.1 The Concept of FF-SAR

Conventional satellite altimetry produces what is referred to as Low Resolution Mode (LRM) data. This radar remote sensing technique involves a satellite emitting microwave signals directed towards the Earth's surface. These signals scatter upon hitting the surface, with a portion reflecting back to the satellite. The reflection strength varies based on surface roughness. Smooth surfaces like water reflect more signal, resulting in a more powerful detected return signal compared to other surfaces [39]. The satellite receives part of the original signal moments after transmission, the time this takes is known as the time delay. The time delay is used to calculate the distance between the satellite and the Earth's surface [22]. The emitted signal spreads out in a cone-like pattern, creating a pulse footprint on the ground [22][34]. This signal contacts the ground and scatters in various directions. Water returns a strong signal power compared to other surfaces. However, the large pulse footprint makes it challenging to precisely pinpoint the exact locations of these bright water signals [22][32].

To enhance the precision and resolution the more recent technique of UF-SAR altimetry, or delay-Doppler altimetry, is applied to obtain altimetry data. It was first operationally used for the CryoSat-2 mission, launched in 2010 [33] [39]. According to [[1],[32],[34]], the UFSAR processing can be summarized as follows: In SAR-altimetry, radar waves (or pulses) are emitted at a higher rate compared to LRM altimetry, around 18000 pulses per second instead of about 2000. Emitting radar waves at a higher frequency ensures that the phase of the signals remains constant across consecutive pulses by minimizing the time between observations, thereby reducing the chance of significant relative motion or environmental changes that could disrupt phase coherence. Maintaining a constant phase across signals allows SAR-altimetry to synthesize a longer aperture, effectively extending the 'length' of the radar antenna. This synthetic aperture facilitates a finer spatial resolution in along track direction. Since the satellite is in motion, ground reflectors scatter back the emitted signals at various Doppler frequencies depending on their along-track locations (either in front, nadir, or behind of the satellite). A Fast Fourier Transform applied to a burst of consecutive reflected pulses discriminates the surface sampled on different Doppler strips on ground. This means each Doppler strip corresponds to a specific range of Doppler frequencies, which can be linked back to specific geographic locations on the ground. UF-SAR processing is usually applied to bursts of 64 pulses. The radar wave footprint is thus split in 64 Doppler strips of about 300-meter wide in the along-track direction. A given Doppler strip is seen in the radar footprint during ∼2.5 seconds, see Fig. 4. Hence, the same Doppler strip on ground can be sampled at different satellite locations, depending on the burst frequency rate of the altimeter. The combination of different samplings of the same Doppler strip allows speckle noise reduction. This method is called the multi-looking. UF-SAR processing altimetry narrows the pulse footprint and increases the along-track resolution, resulting in the UF-SAR product with an improved along-track resolution of 300 m. This allows for increased number of WSE measurements, enabling the creation of altimetry point profiles at river crossings [30]

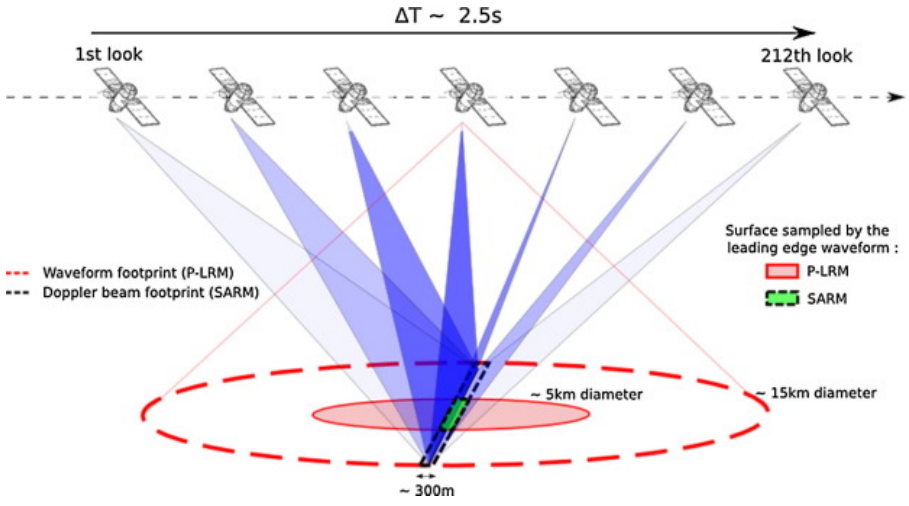

Figure 4: Evaluation of SAR altimetry from CryoSat-2 acquisitions [5].

The missions CryoSat-2 and the Sentinel-3 were designed for UF-SAR processing, where only bursts of radar pulses are coherently processed together, corresponding to a relatively short integration time (∼3 ms). For UF-SAR, the shorter integration time is a trade-off, balancing resolution with processing complexity. In FF-SAR, by extending the integration time up to ∼2.5 seconds by including the entire illumination period, the system can significantly enhance the along-track resolution. By increasing the synthetic aperture (integration time), the achievable Doppler resolution is refined and thereby the ground resolution in along-track. Sentinel-6 is best suited for FF-SAR due to open burst operation that allows for a more continuous emission and reception of radar pulses [14] [1]. The along-track resolution follows from Eq. 1;

$$L = 0.886 \frac{cR_0}{2 f_c v_s T_i} \tag{1}$$

With the along-track resolution L, speed of light in a vacuum c, the tracker range distance from the radar to a target at the closest point of approach R_0, carrier frequency f_c, and the velocity of the satellite v_s. T_i represents the coherent integration time, in the case of UF-SAR it is the burst duration (∼3 ms), for FF-SAR this value corresponds to the scatterer illumination time (∼2.5 s). This higher value of T_i leads to a lower value of L, thus an improved along-track resolution up to ∼1.0 m [14].

As a result, the footprint from FF-SAR is a narrow strip on the surface, useful for applications that require separating specific targets within highly heterogeneous scenes, such as rivers in the complex topography of BNP. With FF-SAR, water surfaces can be located more precisely along-track and appear with greater contrast within the radargram. Radargrams from the different altimetry techniques for the Garonne river in France are illustrated in Fig. 5, where the improved spatial resolution results in a clearer returned power signal from the river. For LRM the signal only gives a bright peak when the river is located close to nadir. When using the higher resolution UF-SAR and FF-SAR products the river signal is not only clearly visible close to nadir, but also in far cross-track locations. Notice in the magnification panels that only FF-SAR can provide a high-contrast river echo in presence of meanders. The increased resolution from FF-SAR can be utilized to derive WSEs from meandering river and smaller water targets [2][8].

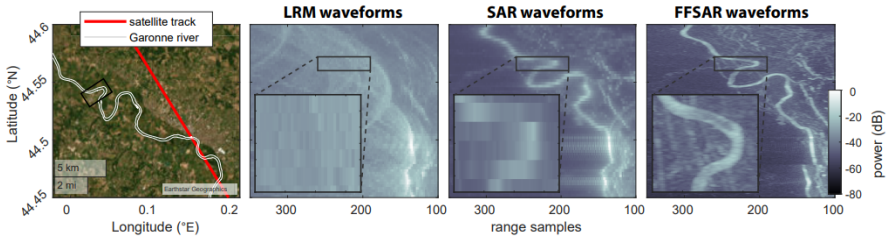

Figure 5: Figure obtained from [2] showing the Garonne river in France as seen in different altimeter data products with varying along-track resolution due to differences in processing. The left image shows the observation geometry. The right images show consecutively the return power signal from LRM, UF-SAR, and FF-SAR.

2.2 Altimetry Data Processing

To obtain FF-SAR data for deriving WSEs involves processing steps across different data levels: Level-1A (L1A), Level-1B (L1B), and Level-2 (L2). Each level represents a stage in transforming raw satellite data from Sentinel-6 into WSEs. These processing steps are illustrated in Fig. 6. This section describes the processing stages, with a focus on the transition from L1B to L2.

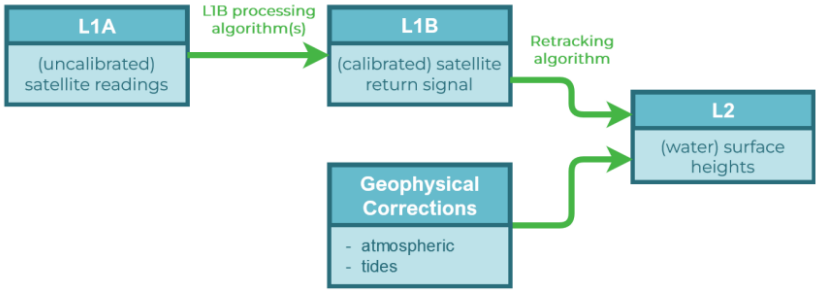

Figure 6: Figure obtained from [11] showing a simplified overview of the SAR altimetry data processing steps based on the EUMETSAT Sentinel-6 altimetry data processing baseline [20].

The input data for level-1 processing consists of level 0 products, which include raw telemetered data, time stamped and with initial geolocation [20]. The primary function of the level-1 processing chain is to calculate the tracker range and generate level-1 waveforms, applying instrumental corrections to all of them. The main input data for level-2 processing are the level 1B altimetry products. The first function of the level-2 processing chain is to apply a retracking algorithm to the level 1B waveforms to calculate the WSEs [2]. The second function of the level-2 processing chain is to compute and apply all geophysical corrections to the measurements. The following sections will describe the FF-SAR (Level-1B) (2.2.1) and Level-2 (2.2.2) data processing in more detail.

2.2.1 FF-SAR Data Processing

In this work, the FF-SAR waveforms are produced via an algorithm as outlined in [14]. The used processing algorithm was first implemented for CryoSAT-2 by [28] and later adapted to the Sentinel-3 and Sentinel-6 missions as well [2]. As outlined in Sec. 2.1, the Doppler frequency resolution (proportional to the along-track ground resolution L) of any SAR-processed altimeter return signal is inversely proportional to the length of the aperture (or equivalently the integration time T_i). Regarding this aspect, the SAR processing can actually be seen as an equivalent to a classical power spectral density estimation from a time series of length T_i: Increasing the length of the sampled time series improves the frequency resolution $df = (T_i)^{-1}$. This simple correspondence underlines that both the classical UF-SAR processing and the FF-SAR processing rely on the same mathematical principles. We set the integration time T_i to ∼2.2 seconds, which yields roughly ∼1 m theoretical range resolution with the Sentinel-6 mission parameters, see Tab. 1;

Variable	Sentinel-6
tracker range R_0 (km)	∼1344.1
velocity v_s (km s^{-1})	∼6.97
burst repetition frequency BRF (Hz)	∼139.26
pulse repetition frequency PRF (Hz)	∼9.195
chirp bandwidth B (MHz)	320
carrier frequency f_c (GHz)	13.575
chirp slope s (10^{12} Hz s^{-1})	∼10
number of pulses in burst N_b	64
burst duration T_b	N_b/PRF

Table 1: List of mission parameters. The values marked with ∼ have been rounded. R_r, v_s, BRF, and PRF are varying over the orbit [2].

While the integration time is the most crucial parameter for FF-SAR processing, there are more options to consider:

- Windowing: Due to the heritage from the underlying Fourier transforms, the point target response in both range and along-track is well-approximated by a sinc^2 function [2]. This function has undesirably high side-lobes, that can deteriorate measurement quality in scenes of high contrast, as is the case for river

echoes. To mitigate these effects it is common practice to apply windowing within the SAR-processing, as illustrated in Fig. 7. We apply a Hamming window in both range and along-track direction, after which the point target response is well approximated by a Gaussian function (thus without the side-lobes). This windowing technically decreases the along-track and range resolution.

- Zero-padding: To mitigate the effects of aliasing, it is common practice to oversample the altimeter signal in the range direction by a factor of 2. Aliasing occurs when a signal is undersampled, causing different signals to become indistinguishable from each other. This can distort the data and lead to inaccuracies. The initial L1A pulse data are reported at range intervals of approximately 40 cm, while the FF-SAR waveforms are sampled at range intervals of approximately 19 cm. Consequently, the Sentinel-6 FF-SAR waveforms contain 512 range samples (range gates), whereas the Level-1A data originally contain only 256 range gates. This procedure aligns with the official UF-SAR processing conducted by EUMETSAT.

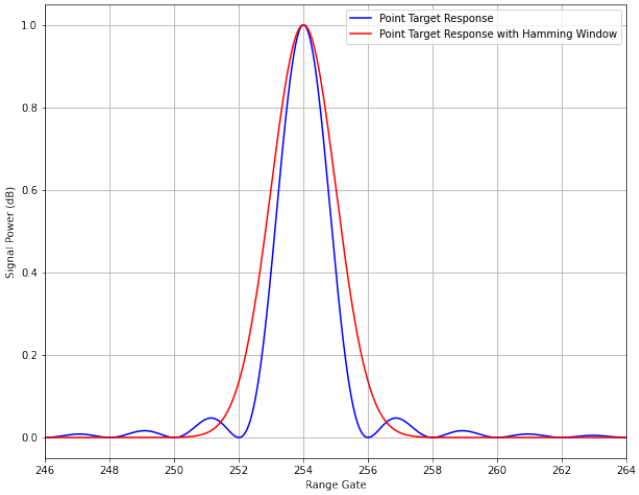

Figure 7: The figure illustrates the point target response for a waveform representing a river, where the river signal occupies a single range gate at 254. The blue line depicts the point target response without applying a Hamming window, which contains side lobes that can deteriorate measurement quality in high-contrast scenes. The red line shows the point target response with a Hamming window, which is well approximated by a Gaussian function.

The final output of the FF-SAR processing is a radargram of return signal power over range and along-track, as illustrated in Fig. 8. Sentinel-6 operates in RMC mode [19], this results in the loss of the tail information (range gates 280-512) by the darker shaded part of the waveforms. As a result, the power signal returned from this section of the FF-SAR image does not yield reliable data for river analysis. Therefore, our analysis will concentrate on river segments situated from range gate 0 to 279.

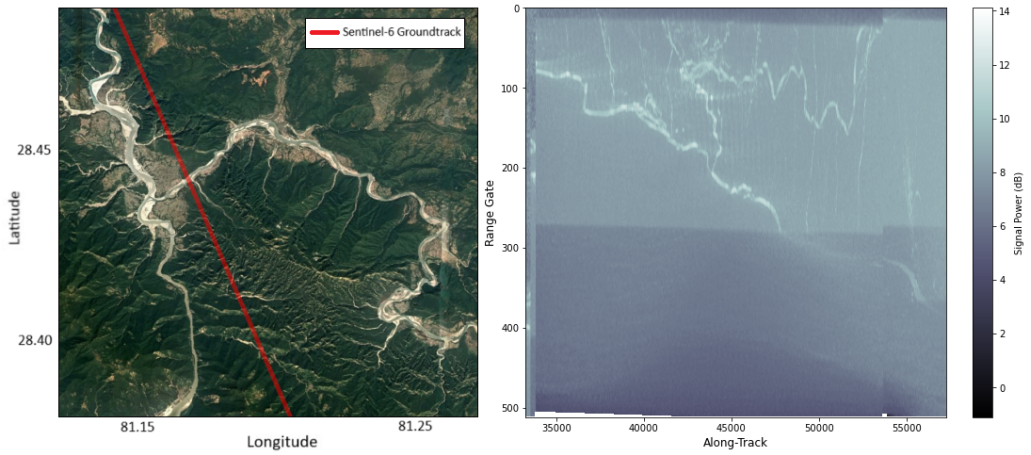

Figure 8: The left figure displays a satellite image of BNP, featuring the Karnali River flowing from the north and the Bheri River from the east. The red line indicates the Sentinel-6 ground track over BNP in Nepal, with the satellite descending during the overpass. The image is sourced from Google Earth. The right figure presents an FF-SAR radargram of the same region, showing a clear returned power signal from the Karnali River between along-track indices 35000 and 45000.

2.2.2 Level-2 Data Processing

Deriving WSEs from Sentinel-6 FF-SAR altimetry data involves the process of waveform retracking. This process determines the range from the satellite to the river surface, from which the WSEs are calculated. When observing different terrains using an altimeter, the behavior of the returned power varies. The shape of the returned power over the range samples (or range gates) is called a waveform and provides knowledge about the surface characteristics. As mentioned before in Sec. 2.1, the reflection varies depending on surface roughness. Smooth surfaces like water reflect a significant portion of the signal back to the satellite, resulting in a strong signal power detected compared to other surfaces. The return signal waveform for rivers typically consists of a single peak, see Fig. 9. This characteristic can be used in waveform retracking to derive river WSEs.

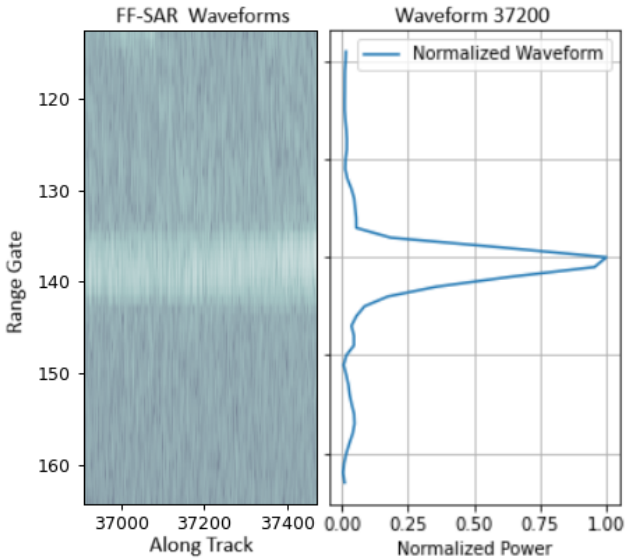

Figure 9: The left figure shows a heat map of the FF-SAR waveforms for the Karnali river in BNP. The right figure shows normalized FF-SAR waveform for index 37200 along track.

In the waveform, the river should give a peak at the range gates corresponding to the river location. The aim of waveform retracking is to determine the range from the satellite to the river [15]. These range values are utilized for the calculation of river WSEs, more detail in Sec. 3.2.1.

However, the Sentinel-6 radar signal used to obtain the waveforms travels through the atmosphere, thus affected by atmospheric delays. The geophysical correction factors to be accounted for are the modelled dry tropospheric correction at measurement altitude, modelled wet tropospheric correction at measurement altitude, ionospheric

delay correction, solid Earth tide correction, polar tide correction, and the modelled instrumental range correction [13]. The mean values of the geophysical corrections at measurement latitudes of BNP are given in Tabel:

Geophysical Corrections	**Mean (m)**
Modelled Dry Tropospheric Correction	-2.215
Modelled Wet Tropospheric Correction	-0.131
Ionospheric Delay Correction	-0.078
Solid Earth Tide Correction	-0.004
Polar Tide Correction	0.004

Table 2: Mean values for the geophysical corrections at measurement latitude of BNP.

The dry tropospheric correction is the largest contributor to the refraction experienced by the transmitted and received signal, caused by the interaction of dry gas components in the atmosphere with the signal. The wet tropospheric correction accounts for the effects of water vapor and liquid water droplets in the atmosphere. At the latitudes of BNP, the value for this correction varies due to the annual precipitation pattern, as illustrated in Fig. 10. The ionospheric delay is caused by the electromagnetic wave propagating through the ionosphere and interacting with free electrons and ions. The solid Earth tide is caused by the gravitational forces mainly from the Moon and Sun, which leads to a vertical displacement proportional to the tidal potential. Finally, the polar tide is a correction for the ocean's behavior to the deviation in equilibrium solid Earth and ocean caused by the change in the rotation axis of the Earth [10]. All these factors are contained in the Level-2 data files and contribute to the total correction. The total correction essentially results in an overestimation of the measured range by Sentinel-6, thus the sum of all geophysical correction is subtracted from the retracked WSE [15].

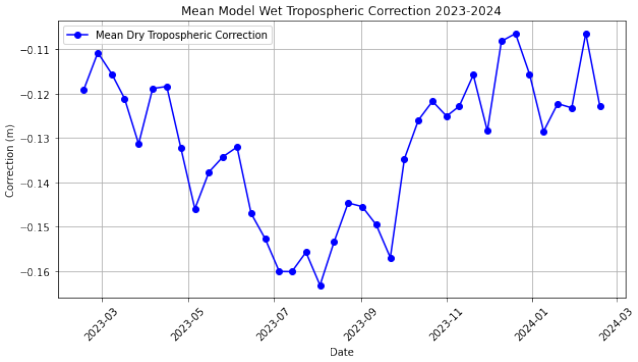

Figure 10: The time series displays the mean model wet tropospheric correction for 2023-2024 at the latitudes of BNP. Due to the high precipitation during the summer monsoon, the wet tropospheric correction values become more negative in the summer months.

3 Data and Methods

In this section, we introduce the datasets and methods used in this work. The datasets include Sentinel-6 data, river polygons and centreline, SWOT data, and in-situ data. We then detail the methods employed to retrieve river water levels, which involve the measurement principles and the PICTA technique for WSEs. Finally, the data analysis section outlines the methods used to address the research question posed earlier, including the process of constructing river level profiles.

3.1 Datasets

3.1.1 Sentinel-6 Data

The Copernicus Sentinel-6 mission is primarily designed to measure sea surface heights, significant wave heights, and inland water heights. The mission includes two satellites. The first satellite, named Sentinel-6A Michael Freilich, is launched on 21st November 2020. Sentinel-6B is scheduled for launch in 2025. Sentinel-6 is in a low earth orbit with a repeat cycle of ∼10 days. The mean altitude is 1336 kilometers with an inclination of 66°, providing coverage of the Earth surface between 66° north and south of the equator. For in-land water heights we are interested in the data from the Poseidon-4 instrument. Poseidon-4 is a nadir-pointing dual frequency SAR altimeter designed to provide high accuracy and high precision altimetry measurements [1]. The data products from Sentinel-6 include the unprocessed waveforms, satellite ground track coordinates, satellite height, and tracker range. The Sentinel-6 data will be processed as outlined in Sec. 2.2. The resulting data products will be used to derive river WSEs with respect to the the reference ellipsoid (WGS-84) [17].

The Sentinel-6 ground track crosses the BNP, covering a section of the Karnali River, illustrated before in Fig. 8. FF-SAR processing enables to retrieve waveforms within an approximately 14 kilometers wide swath centered around the satellite's ground track [14]. With this swath width, Sentinel-6 effectively captures nearly the entire region depicted in the figure. The corresponding FF-SAR radargram has 512 range samples in cross-track direction over 20000 waveforms in along-track direction (equal to approximately 20 km), illustrated before in Fig. 8. The Sentinel-6 radar altimetry data is obtained from the EUMETSAT Datastore. The obtained Level-1A data is the most recent reprocessed data product from the collection "Poseidon-4 Altimetry Level 1A High Resolution (baseline version F08) - Sentinel-6 - Reprocessed". The geophysical corrections are obtained from the associated Level-2 product "Poseidon-4 Altimetry Level 2 High Resolution (baseline version F08) - Sentinel-6 - Reprocessed". The filenames include information about the sensing period, relative orbit, and cycle numbers, example for 2024-02-18 is illustrated in Tab. 3. The dataset spans from 2023-02-16 to 2024-02-18, with the satellite revisiting the area every 10 days, resulting in a total of 38 files collected over this period.

File Identifier
S6A_P4_1A_HR_____20240218T021251_20240218T030908_20240310T131958_3377_120_192_096_EUM__OPE_NT_F08
S6A_P4_2__HR_STD__NT_120_192_20240218T021253_20240218T030906_F08

Table 3: EUMETSAT filenames for Sentinel-6 Level-1A and Level-2 High Resolution data for 2024-02-18.

This study focuses on the segment of the Karnali River between latitudes 28.40° and 28.50°. The river segment is of great interest for several reasons. First, this river segment includes the Chisapani river level gauge station that is active since 1992 [12]. Second, it includes the bifurcation of the Karnali River from the north-west and the Bheri River from the north-east. Finally, the Karnali River before and after the bifurcation is meandering in along-track direction (parallel to the ground track). The work of [15] shows that the accuracy of the obtained WSEs is generally highest for river segments that are directed parallel to the ground track and becomes worse with increasing inclination.

3.1.2 River Polygon and Centerline

Besides the FF-SAR waveforms, PICTA requires a river polygon [15]. A polygon is a plane figure composed of line segments connected to form a closed chain. The river polygon data consists of a series of longitude and latitude coordinates that outline the area covered by the river. The river polygon for our segment of interest in the Karnali River is illustrated in Fig. 11. To create river level profiles over long distances, it is essential to utilize multiple river polygon segments. This segmentation is required because the algorithm for retrieving river level profiles needs an initial guess for the height and slope of the river [15]. Without dividing the river polygon into sections, this initial guess cannot accurately represent the river due to the significant variations in height and slope in the complex topography of BNP. The river polygons are obtained from the mapping database OpenStreetMap as KML files. In OpenStreetMap, the river polygons are outlined by the government

of Nepal [12]. However, using a static polygon from OpenStreetMap does not consider the changing extent of the river width varying over time, more detail is provided in Sec. 3.3.4.

To create river level profiles, we need to map the derived WSEs onto the river centerline (see Sec. 3.3.2). The river centerlines are also obtained from the mapping database OpenStreetMap as KML files. The files contain coordinates of the centerline points approximately every 10 m. These are converted to a continuous line representing the centerline of the river (see Fig. 11).

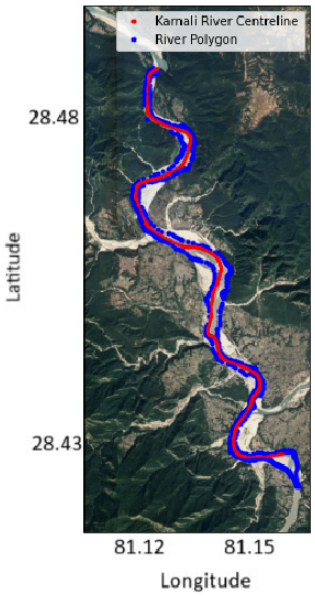

Figure 11: Polygon and centerline for a segment of the Karnali River in Bardiya National Park, Nepal.

3.1.3 SWOT Data

The SWOT mission conducts a global survey of the Earth's surface water, collecting detailed measurements of how water bodies change over time [6] [3]. The mission's primary instrument is the Ka-band Radar Interferometer (KaRIn), an advanced near-nadir viewing interferometric altimeter. KaRIn features two distinct 50 km swaths and utilizes two SAR antennas, enabling a swath width of approximately 120 kilometers on the Earth's surface. It sends radar pulses that bounce off the water's surface and then captures the return signals with its antennas. Unlike the nadir altimeter, which points straight down and gathers one-dimensional data, KaRIn's antennas are tilted to scan the surface in two dimensions, offering higher precision. KaRIn boasts a range resolution of about 10 meters and an elevation accuracy of approximately 0.5 meters. The satellite surveys the globe between 78° N and 78° S latitude, covering around 90 percent of the planet's surface. The frequency of repeat observations at any given location during the 21-day repeat orbit varies with latitude [18]. BNP, for instance, has one observation every 21 days.

The KaRIn global High Rate (HR) hydrology products that are currently available can be accessed via the Hydroweb Portal. From this portal, we obtained the Level 2 KaRIn high rate water mask pixel cloud product (L2_HR_PIXC). This product contains measured height (with respect to WGS-84), geolocation, and classification data from the high-rate (HR) data stream of the KaRIn instrument. These data are generally produced for inland and coastal hydrology surfaces. The heights from the L2_HR_PIXC for a segment of the Karnali River are shown in Fig. 12. The pixel cloud data points have a spatial resolution of approximately 20 m [3]. The HR hydrology products from SWOT are recently obtained, with the date range from 2024-01-25 to 2024-03-06 [31], providing two observations for that period.

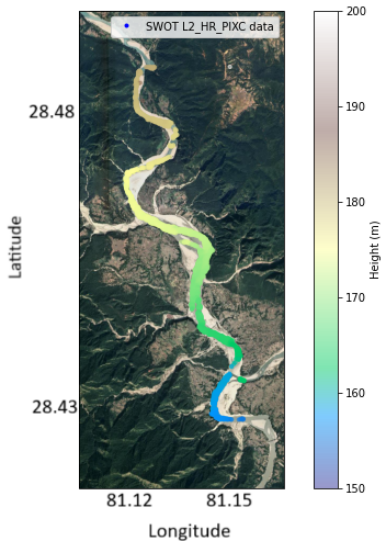

Figure 12: Level 2 KaRIn high rate water mask pixel cloud height product for a segment of the Karnali River with respect to WGS84.

3.1.4 In-situ Data

The Chisapani water level river gauge is an automatic in-situ measurement station for WSEs of the Karnali River [4]. The WSEs are provided with respect to an unknown local reference frame, with measurements taken every 15 minutes [12]. Water surface height data from this gauge is available for the period from 1992 to 2018, allowing us to calculate the mean WSE over that time span. The time series in shown in Fig 25. The data was shared with TU Delft by the government of Nepal. This long-term WSE time series enables an indirect comparison with the PICTA derived WSEs.

3.2 PICTA method for River WSEs

This section first outlines the measurement principles that form the background for the retrieval of river WSEs. Secondly, we implement the PICTA algorithm from [2], utilizing FF-SAR data and the river polygon to retrack the river WSEs. The algorithm is created anew in Python utilizing ChatGPT [9].

3.2.1 PICTA Measurement Principles

The measurement principle outlines how to calculate the water level of a cross-track river segment, following the PICTA method [2]. We first consider an individual river bank in the side view of Fig. 13. The equations describing the geometry for a spherical Earth are;

$$R_r^2 = (H_s - y_r)^2 + x_r^2, \tag{2}$$

$$y_r = (H_r + R_E)\cos\phi_r - R_E, \tag{3}$$

$$x_r = (H_r + R_E)\sin\phi_r. \tag{4}$$

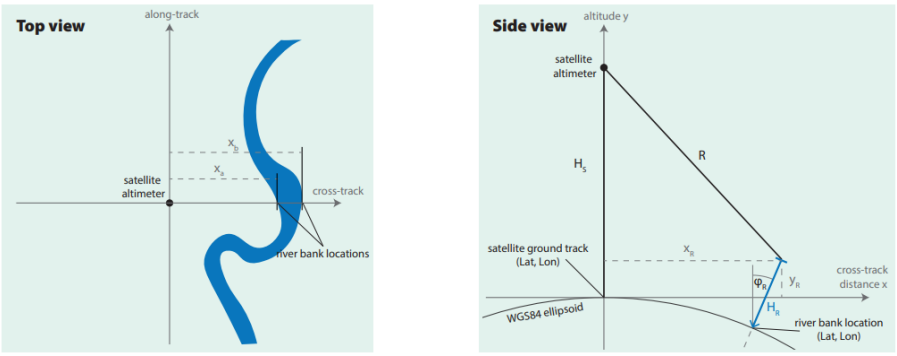

Figure 13: Observation geometry sketch. Top view on the left-hand side, showing the cross-track distance to the river bank locations of a meandering river. Side view on the right-hand side, showing the water surface elevation H_r, and the variables to take into account Earth's curvature for cross-track altimetry [15].

Here, R_r is the slant range measured by the altimeter, representing the line-of-sight distance from the satellite to a point on the Earth's surface. H_s is the altitude of the satellite above the Earth's surface. The along-track distance y_r and the cross-track distance x_r to the river banks are estimated using river polygons. R_E is the Earth's radius. ϕ_r is the angle in radians, measured from the Earth's center, between the nadir point and the location of interest on the Earth's surface. This angle is used to calculate the along-track and cross-track distances. H_r is the Water Surface Elevation (WSE) of the river.

However, the proportions in Fig. 13 are greatly distorted because H_r (∼100 meters) and x_r (∼7 kilometers) are small compared to Earth's radius R_E (∼6371 kilometers) and satellite altitude H_s (∼1336 kilometers). This means that ϕ_r is very small, and H_r is almost aligned with the y-axis, allowing for simplifications [15]. Therefore, the water surface elevation H_r can be approximated with Eq. 5;

$$H_r = H_s - R_r + \frac{x_r^2}{2H_s} + \frac{x_r^2}{2R_E} = H_s - R_r + Kx_r^2 \tag{5}$$

where $K = \frac{1}{2H_s} + \frac{1}{2R_E}$. Eq. 5 allows for the calculation of cross-track water levels along the river. To calculate H_r, values for the river's cross-track distance x_r are required. Since K is a small value, relatively large errors in x_r can often be tolerated without significantly affecting the accuracy of the resulting river WSE.

So far, we have considered a single cross-section associated with an individual waveform that contains a single target at range R_r and cross-track distance x_r, as sketched in the side view of Fig. 13. However, rivers are extended targets, as shown in the top view of Fig. 13. Therefore, at least two ranges can be extracted from one waveform with the following interpretation: the rise of the altimeter signal corresponds to the range to the closest river bank (onset), while its decay provides the range to the farthest river bank. Utilizing Eq. 5, we can calculate the WSEs at both river banks. The water level of the river segment can finally be calculated by averaging the WSEs from both river banks.

3.2.2 PICTA Algorithm for River WSEs

This subsection presents the algorithm to retrack river WSEs utilizing FF-SAR data and river polygons, based on the measurement principles. It provides a detailed description of the main processing steps for a single FF-SAR data file. This process can be repeated for all FF-SAR data files to determine the WSEs of a river segment over time. The steps of the PICTA algorithm are based on the method detailed in [2].

i) First, we read the data for a single overpass over BNP. This data includes the FF-SAR waveforms (Fig. 8), and the Sentinel-6 ground track coordinates, altitude, and tracker range. The FF-SAR data can be sliced according to the river segment of interest to optimize computational efficiency. Next, we read the river polygon for the segment of interest (Fig. 11).

ii) The objective of the second step is to calculate the cross-track distances x_r between the satellite ground track and the river banks from the river polygon. The process begins by projecting the river polygon into a local Cartesian East-North-Up (ENU) coordinate system, assuming zero elevation ($H_r = 0$). The coordinate transformation is crucial for positioning the river within the same coordinate system as the satellite data. Following this, the FF-SAR footprint is approximated as a line segment oriented in the cross-track direction and centered around the origin of the local ENU coordinate system. The footprint is a line perpendicular to the satellite ground track. Every 10 meters along the satellite ground track, the intersections of this footprint line with the projected river polygon is then determined within the East-North plane. This process provides the East and North coordinates of all intersected river banks. The river's possible meandering paths might lead to multiple intersection points per footprint. For each identified intersection point, the Euclidean distance from these points to the origin of the ENU coordinate system is computed, providing the cross-track distances x_r. The coordinates of intersection points (E_r, N_r, $H_r = 0$) are transformed back into ellipsoidal (geodetic) coordinates. This conversion is necessary to obtain the altitude offsets at the off-nadir positions due to the ellispoid's curvature [15]. These altitude offsets yr_0 replaces the term $\frac{x_r^2}{2R_E}$ for a round Earth in Eq. 5.

iii) Following this step, Eq. 5 can be rewritten to calculate the slant range R_r. To solve for R_r, an initial guess of the WSE $H_r = H_0$ has to be given. The WSE of a river typically varies much less than the width of the altimeter's receiving window (approximately 100 meters). Therefore, the initial guess for the river WSE was determined using Google Earth. The calculated slant ranges R_r are used to calculate the range gate index at which to expect the river banks, see Fig. 14;

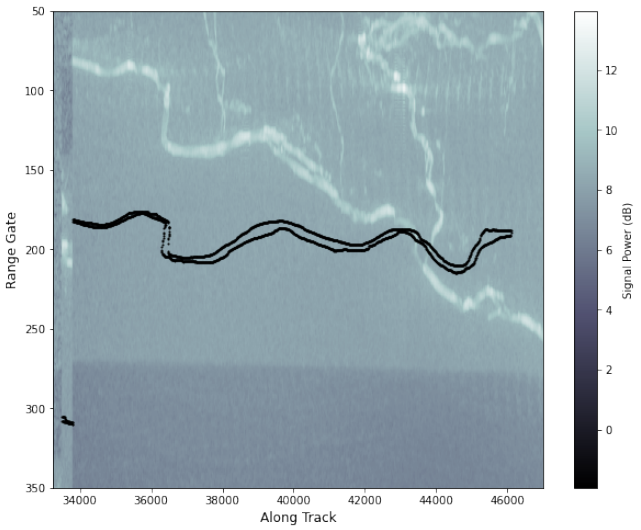

Figure 14: Initial guess of the river bank ranges in the FF-SAR waveforms.

iv) The aim of this step is to optimize the detection of the river signal within the FF-SAR waveforms. For this optimization process, we utilize an offset H_0 and slopes along the river's centerline distance dH_{lon} and dH_{lat} to model the river's elevation. The range samples at which the river banks are detected $r = r(H_0, dH_{lon}, dH_{lat})$ are modeled as functions of these variables. This allows for the identification of minimum and maximum ranges for each river intersection within a waveform. The log-power of the waveforms $\log_{10}(P_{i,r})$ (with waveform index i and range sample r) should be high between those range samples due to the river signal.

The objective is to maximize the log-power of the waveforms with respect to H_0, dH_{lon}, and dH_{lat}. Specifically, we maximize:

$$\max_{H_0, dH_{lon}, dH_{lat}} \sum_{r=r_{i,\min}-r_{\text{buffer}}}^{r_{i,\max}+r_{\text{buffer}}} \log_{10}(P_{i,r}). \tag{6}$$

This method seeks to maximize the log-power of the waveforms, calculated as $\log_{10}(P_{i,r})$. Using log-power ensures robustness against the varying amplitude of the river signals, which may fluctuate because of the varying cross-track distance between the satellite's ground track and the river banks. The optimization incorporates a buffer of multiple range samples to accommodate the finite width of the point target response [15] and to compensate for inaccuracies arising from the assumption of linear slopes in elevation. This optimization process results in Fig. 15. Part of the river signal is not within the polygon, in the next step we account for this by creating a buffer around the polygon river bank ranges.

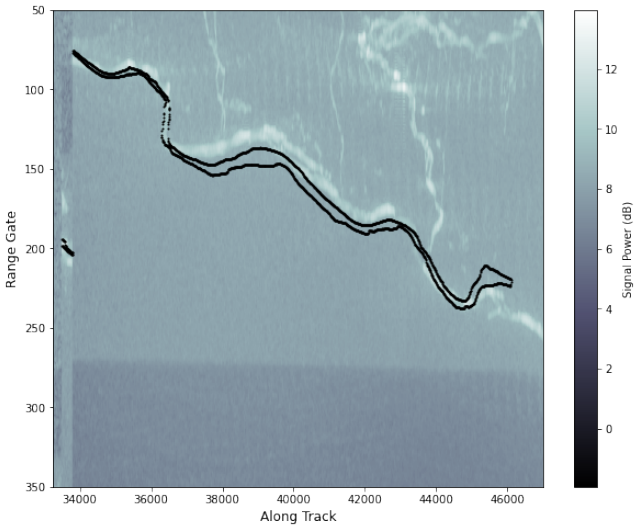

Figure 15: Optimized guess of the river bank ranges in the FF-SAR waveforms.

v) The next step consists of two parts. First, the waveforms are smoothed to reduce noise by averaging them over a moving window of 10 range samples in the along-track direction. The second part involves creating cropped waveforms (called subwaveforms), which are segments of the waveforms that supposedly contain the river signal for further processing. This minimizes the inclusion of clutter (other bright signals within the scene that are not part of the river, such as other water bodies) in the actual retracking process. Each subwaveform is obtained by creating a buffer of 10–20 range samples around the range gates shown in Fig. 15. The resulting subwaveforms are illustrated in Fig. 16. For meandering rivers (in cross-track direction), we may identify multiple subwaveforms per waveform.

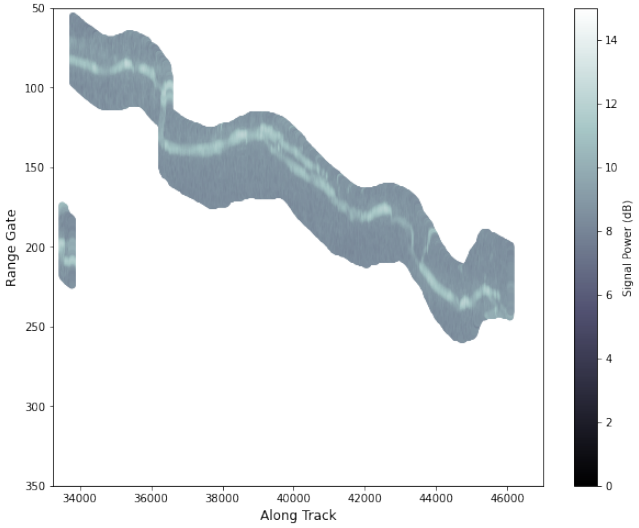

Figure 16: FF-SAR subwaveforms.

vi) The aim of this step is to retrack the range gate values corresponding to the river banks. First, each subwaveform is normalized by dividing it by its maximum value. The normalized subwaveforms are then retracked using a threshold retracker applied at $x = 0.1$ [15]. Normalizing the waveforms and applying the threshold is done to minimize the identification of clutter. Finally, the peak with the highest power per range sample is used to retrack the range gate values of the two river banks. The onset (blue line) and decay (red line) are determined by detecting the intersection points under the highest peak between the threshold line and the normalized subwaveform, as shown in Fig. 17;

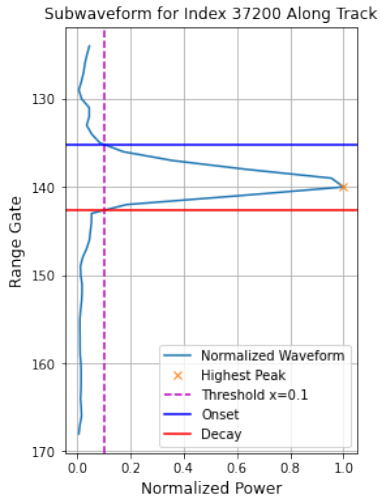

Figure 17: Normalized FF-SAR subwaveform at satellite index 37,200. The onset (blue) and decay (red) are obtained by detecting the intersection points under the highest peak (yellow cross) between the dashed threshold line $y = 0.1$ (purple) and the normalized subwaveform (blue).

The onset of the waveform signal corresponds to the range to the closest river bank, while its decay provides the range to the farthest river bank [15]. The algorithm may fail to detect the onset and decay if the peak is situated at the boundaries of the subwaveform; these cases must be disregarded. All subwaveforms are retracked to determine the resulting range gate values for the river banks, as shown in Fig. 18;

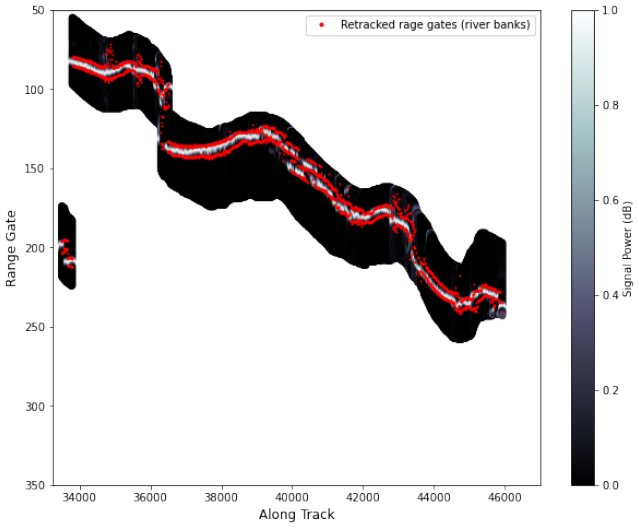

Figure 18: Normalized FF-SAR subwaveforms with the retracked ranges for the river banks.

vii) In this step the resulting ranges are adjusted for the atmospheric delays and tidal variations contained in the Level-2 data files. These correction are described in Sec. 2.2.2. The ranges R_r are adjusted by summing all the geophysical corrections and subtracting this total correction from the ranges. Since the total correction is a negative value (Tab. 2), this results in an increased WSE (Eq. 5).

viii) To calculate the WSE of the river banks, the range gate values corresponding to each river bank are used as input x_r with corresponding adjusted range R_r in Eq. 5. The WSE values from both river banks are averaged

to estimate the WSE for that segment of the river [15]. Similarly, the river bank coordinates are averaged, resulting in a single coordinate with the corresponding WSE approximately every 10 meters along the river segments as the output of the retracking process.

ix) In the final step, quality flags are evaluated to exclude erroneous measurements. First, the retracked ranges are flagged based on the width of the river signal. The retracked width of the river signal, denoted as $\Delta r_{\text{retracked}}$, is the difference between the river bank range gate values. This is compared to the corresponding expected river signal width Δr^* from the optimized first guess (Fig. 15). A small buffer is added to Δr^* to account for the blurring due to the point target response in range, then it can be compared to $\Delta r_{\text{retracked}}$. The WSE is flagged as invalid if the difference between them becomes too large, specifically if:

$$|\Delta r_{\text{retracked}} - (\Delta r^* + 3)| > 4 \tag{7}$$

This criteria ensures that river signals that are erroneously too narrow (such as those caused by noise) or excessively wide (due to additional clutter around the river banks) are flagged as invalid. Additionally, this criterion marks estimates as invalid when the river significantly overflows its banks during high-water conditions, thereby ensuring that only signals with a reasonable width are considered valid [15]. The result is illustrated in the left image in Fig. 19.

Furthermore, overlapping range gates present the second flagging condition. When subwaveforms overlap, often occurring near the nadir or within river bends, multiple river echoes might be detected within a single subwaveform. This overlap can lead to ambiguity in selecting the correct peak for slant range corrections, as either of the peaks may be chosen. Consequently, in such situations, we cannot accurately retrack the WSE, leading to the WSE being flagged as invalid, as illustrated in the right image in Fig. 19.

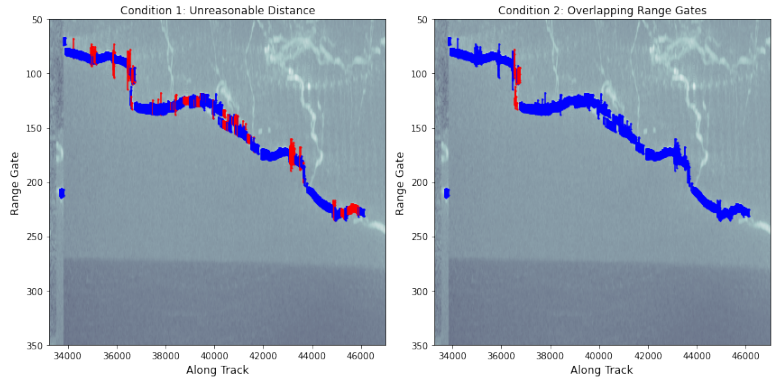

Figure 19: The criteria for quality flags for the retracked WSE are shown, with blue indicating valid and red indicating invalid data. The left figure validates range gates based on the relationship between $\Delta r_{\text{retracked}}$ and Δr^* to identify unreasonable distances. The right figure validates range gates based on criteria for overlapping range gates.

x) To detect outliers in the obtained WSEs, we apply the rolling z-score method [38] [25]. This method detects outliers in FF-SAR data by calculating a z-score for each data point using the subset of data points within a rolling window. The window is centered at the data point in question. The z-score is the difference between the height at a point h_i and the local mean μ_{local}, divided by the local standard deviation σ_{local}. If the z-score of a point is below a predetermined threshold, that point is considered as valid. The method is also applied to the SWOT dataset for consistency. In doing so, we use the same rolling window and threshold.

3.3 Analysis of River Level Profiles

This section describes how the research questions will be assessed based on the retrieved WSE. There are four subsections corresponding to the four research questions.

3.3.1 Analysis of PICTA and In-Situ WSE time series

For the first research question, we aim to assess the agreement between in-situ and PICTA derived WSE time series. The agreement will be evaluated by comparing the WSE from FF-SAR (2023-2024) with the water surface height measured at the Chisapani station (1992-2018). To perform this comparison, we select the closest PICTA derived WSE data points within a maximum radius of 100 meters around the Chisapani station. Fig. 20 shows the FF-SAR data points and the two locations of interest, marked by circles each with a radius corresponding to the maximum allowable distance.

Figure 20: FF-SAR data points for a segment of the Karnali River in Bardiya National Park, Nepal. The locations of Kuine Bridge (red) and Chisapani river gauge station (green) are illustrated with circles representing the maximum allowable distance for the FF-SAR points.

The WSE data from Sentinel-6 measurements are taken approximately every 10 days [17], in contrast to the in-situ measurements, which are taken every 15 minutes. Nevertheless, the PICTA derived WSEs are expected to follow the same seasonal trends as the in-situ measurements, demonstrating similar differences between high and low water seasons, with the highest water levels observed in the summer months [26]. Additionally, we also create a WSE time series for an upstream location at Kuine Bridge. Although there may be differences in WSE values due to varying geography, the time series for this upstream location should exhibit seasonality patterns consistent with those observed at Chisapani, with an offset reflecting its upstream position on the Karnali River.

3.3.2 Analysis of PICTA and SWOT River Level Profiles

For the second research question, we aim to assess the agreement between SWOT and PICTA derived river level profiles. The points (latitude, longitude) at which WSE is measured by PICTA and SWOT typically do not coincide with the river centerline. Hence, to generate a river water level profile, we first project the measured data onto the centerline. This projection is achieved by calculating the closest distance from the each data point to the river centerline. This gives the corresponding distance along river centerline to the water surface height. The projection aligns WSEs from PICTA and SWOT both to the same reference frame, represented by water surface height over the distance along the river centerline. The points are then sorted based on their projected distances along the centerline, with the downstream endpoint of the river segment defined as zero distance.

We will construct river level profiles from PICTA and SWOT data for a segment of the Karnali River, as shown

in Fig. 11. This segment is covered by both SWOT and Sentinel-6, allowing for a direct comparison of the derived profiles. The selected Sentinel-6 overpasses are the ones closest in date to those from SWOT to ensure the comparisons are temporally coherent. Once both river water level profiles are generated, their agreement can be assessed by comparing the nearest neighboring points. Again, a maximum allowed distance of 100 m is set to ensure that the compared data points represent the same location on the river. To quantify the agreement, two metrics are used:

- Unbiased Root Mean Square Error (RMSE): This metric provides insight into the consistency between the WSE points obtained from SWOT and PICTA. Lower unbiased RMSE values indicate higher agreement and less deviation between the datasets. While it primarily assesses overall accuracy, it can be influenced by outliers [24]. To assess the differences between both datasets, we quantify the bias and spread, respectively described by the mean bias and unbiased RMSE:

$$z = \sum_{i=1}^{n} (h_i^{PICTA} - h_i^{SWOT}), \tag{8}$$

$$\text{mean bias} = \langle z \rangle, \tag{9}$$

$$\text{unbiased RMSE} = \sqrt{\langle (z - \langle z \rangle)^2 \rangle}. \tag{10}$$

- Scaled Median Absolute Deviation (MAD): Metric equivalent to the standard deviation (unbiased RMSE) in the case of a Gaussian distribution [16]. The scaled MAD is more robust as it is based on median values, ensuring that extreme values do not overly influence the assessment [16].

$$\text{Scaled MAD} = 1.4826 \cdot \text{median}(|z - \text{median}(z)|) \tag{11}$$

The differences z will be visualized by a histogram. Additionally, to assess the influences of the river polygon on the comparison, the PICTA WSEs are derived by utilizing the river polygon obtained from SWOT. This polygon is created by manually outlining a polygon around the SWOT data points. Again, the metrics will be calculated to quantify the influence of the river polygon on the comparison.

3.3.3 Analysis of River Level Profiles over Time

For the third research question, we aim to assess how the river level profiles change over time. We will also analyze and interpret these profiles in relation to river dynamics, establishing a connection between the measurements and river behavior. For each Sentinel-6 overpass from 2023-02-16 to 2024-02-18, a total of 38 river level profiles were obtained. We will generate time series from the river profiles to analyze variations in WSE fluctuations at different locations along the Karnali River segment. These time series will be used to examine the relationship between WSE fluctuations and river geometry.

3.3.4 Analysis of WSE Uncertainty over Time using a Static Polygon

For the fourth research question, we aim to analyze the contribution of the usage of a static polygon to the overall uncertainty. Differences between the static river polygon and the actual river impact the retracked WSEs. Sentinel-2 data (obtained from Sentinel Hub), shows that the Karnali River can double its width during monsoon seasons, leading to significant discrepancies with the static river polygon. PICTA allows us to estimate the river width from the FF-SAR data. By calculating the difference between the river width estimated from PICTA and the static river polygon at the same location, we can establish WSE bounds over time, as will be elaborated below.

The cross-track river width from the polygon is calculated by the difference in x_r between river bank a and b: $w_c^{polygon} = x_b - x_a$, with $x_b > x_a$. To obtain the corresponding cross-track width from PICTA, we use the formula for the Range R_r:

$$R_r = R_{tracker} + (i - 256) \cdot \delta r \tag{12}$$

Here, $R_{tracker}$ is known from the altimeter, δr is the range sampling of $\sim$19 cm, and i is the retracked river bank range gate index. The value 256 indicates the reference range gate index in the center of each waveform. Since most variables in the equations for WSE (Eq. 5) and R_r (Eq. 12) are identical for the two river banks (constants), they can be reduced to the following equation;

$$i \cdot \delta r = K \cdot x_r^2 + C \tag{13}$$

Here, C represents the constant variables. This Eq. 13 presents how the range gate index is altered by the cross-track distance. Since the cross-track river width is calculated as the difference between the river banks x_r, we will fill in Eq. 13 and take the difference between river bank b and a. This results in the following Eq. 14 for the retracked river width:

$$w_c^{\text{PICTA}} = \frac{\delta r(i_b - i_a - w_{ptr})}{2K\bar{x}} \tag{14}$$

Here, $(i_b - i_a)$ is the difference between the retracked range gate index of river banks b (decay) and a (onset). w_{ptr} is an additional fraction that reduces the retracked river width w_c^{PICTA}. $\bar{x}$ is the average cross-track position, representing the cross-track distance of the river segment center to the satellite ground track.

w_{ptr} originates from the overestimation of $(i_b - i_a)$ during the retracking process due to the point target response with a Hamming window, as detailed in Sec. 2.2.1. Applying a Hamming window decreases the along-track and range resolution. As illustrated in Fig. 7, even if a river occupies a single range gate index, retracking the range gates from the waveform results in a difference $(i_b - i_a) > 1$ for a threshold $x = 0.1$. The function of w_{ptr} is to correct this overestimation. The exact value of w_{ptr} will be adjusted based on the resulting w_c^{PICTA}, which is compared with the width from Sentinel-2, assumed to be the true river width. Sentinel-2 data uses the Normalized Water Difference Index (NWDI) to measure the river width in the cross-track direction, as depicted in Fig. 33 in the Appendix.

$\bar{x}$ is the average cross-track position, calculated by taking the average of the cross-track distances x_b and x_a from the river polygon. When $\bar{x}$ approaches zero, w_c^{PICTA} becomes unrealistically large, implying that we can only accurately retrack the river width for cross-track located rivers. To determine the accuracy of estimating w_c^{PICTA} for a section of the Karnali River, we approximate the propagation of the standard deviation of w_c^{PICTA} using the following equation:

$$\sigma_{w_c^{\text{PICTA}}} = \frac{\sigma_r}{2K\bar{x}\sqrt{N}} \tag{15}$$

Here, the factor $\sigma_r = \delta r(i_b - i_a)$ is assumed to be 20 cm, allowing for the algorithm to be off by approximately one range gate for $(i_b - i_a)$. $\sqrt{N}$ represents the number of points over which the average is calculated. The standard deviation is illustrated in Fig. 21, demonstrating the importance of considering the cross-track distance when calculating w_c^{PICTA}.

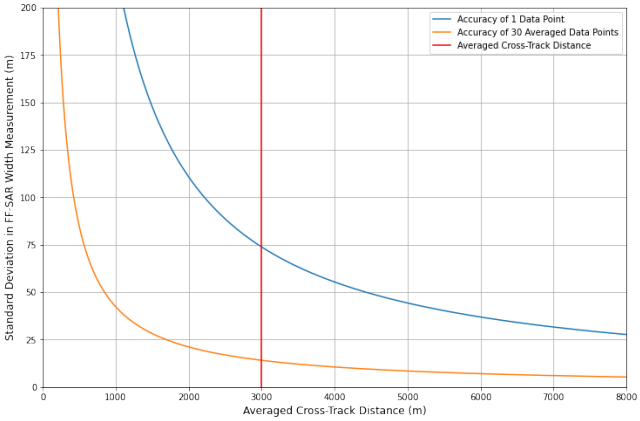

Figure 21: Standard deviation of the retracked river width, with $\bar{x}$ on the x-axis and $\sigma_{w_c^{\text{PICTA}}}$ on the y-axis. The red line indicates an example where a section of the Karnali River is located at 3000 m cross-track, with averaging over 30 data points from a 300 m section, resulting in $\sigma_{w_c^{\text{PICTA}}} = 14$ m.

We can now construct a time series of cross-track river width, including the cross-track width from the polygon (w_c^{polygon}), the retracked river width (w_c^{PICTA}) with error bounds based on the standard deviation ($\sigma_{w_c^{\text{PICTA}}}$), and the river width from Sentinel-2, with error bounds assumed to be 10 m due to measurement errors.

The cross-track widths from w_c^{polygon} and w_c^{PICTA} provide the total range of x_r and can be used to calculate the upper and lower bounds for the WSE. There are three possible scenarios, as illustrated in Fig. 22. In the first scenario, we assume the value of x_b to be true, as per Eq. 5, while the value of x_a is assumed to be skewed, as per Eq. 16. The WSE is the average of H_a and H_b. Since generally $w_c^{\text{polygon}} > w_c^{\text{PICTA}}$, this scenario provides the upper bound. In the second scenario, we assume the value of x_a to be true, as per Eq. 5, while the value of

x_b is assumed to be skewed, as per Eq. 17. This scenario provides the lower bound. In the third scenario, the WSE is calculated using Eq. 5.

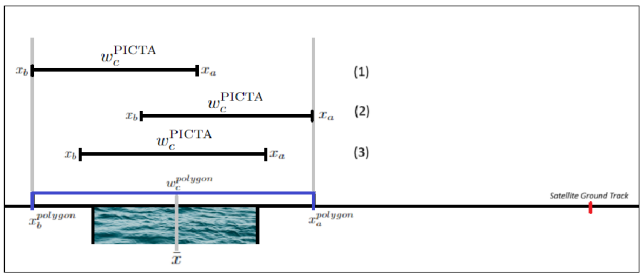

Figure 22: Sketch illustrating three possible scenarios for the retracked river banks compared to the river banks from the polygon. In the first scenario, the retracked river banks are skewed away from the satellite track. In the second scenario, the retracked river banks are skewed towards the satellite track. In the third scenario, the retracked river banks are centered above the river polygon.

$$\hat{H}_a(x_a^{polygon} - w_c^{\mathrm{PICTA}} + w_c^{polygon}) = H_s - R_r + K \cdot x_a^2 \tag{16}$$

$$\hat{H}_b(x_b^{polygon} + w_c^{\mathrm{PICTA}} - w_c^{polygon}) = H_s - R_r + K \cdot x_b^2 \tag{17}$$

The result is a time series that includes the PICTA derived WSEs with upper and lower bounds for a section of the Karnali River. These bounds depend on the difference between the cross-track river width estimated from PICTA and the static river polygon. This allows us to analyze the WSE bounds, representing the uncertainties induced by using a static river polygon for a dynamic river.

We focus on a 100 meter section of the Karnali River, located at 4000 m distance along the river, as shown in the left image of Fig. 27. The section is located approximately 3000 m cross-track. To assess the WSE uncertainty over time, we first need the retracked PICTA river widths w_c^{PICTA}. For each date, the PICTA river width is calculated according to Eq. 14, with the corresponding uncertainty accounted for by the standard deviation calculated using Eq. 15. The number of data points N over which we average is approximately 10, according to the 10 along-track samples per 100 m. The value of $w_{ptr} = 3.5$, is determined based on the expected river width from Sentinel-2, adding an offset to the resulting w_c^{PICTA}.

4 Results and Discussion

This section presents and discusses the results of the analysis described in Sec. 3.3.4.

4.1 PICTA and In-Situ WSE time series

We observe that there are not many PICTA data points retracked close to the Chisapani station, as illustrated in Fig. 20. Since the river signal falls between range gates 280 and 512, an area with compromised data coverage resulting from the RMC mode of Sentinel-6 [19]. Consequently, the FF-SAR waveforms yield unreliable WSE information at this location. However, this issue does not affect the FF-SAR data at Kuine Bridge, which is situated directly upstream of Chisapani. Given the geographical positioning of Kuine Bridge relative to Chisapani, we expect an elevation offset between the two locations. Considering that the mean slope of this river segment over time is approximately 0.001 m/m and the distance along the river centerline between Chisapani and Kuine is about 10 km, an elevation difference of around 10 meters is anticipated. The WSE time series for Kuine Bridge is illustrated in the following Figure:

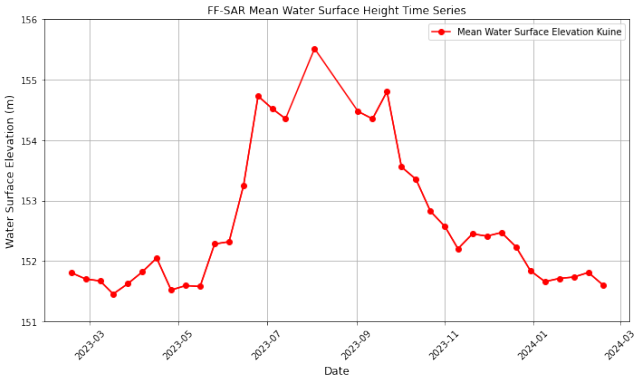

Figure 23: Time series for PICTA derived water surface elevations above WGS84 at Kuine bridge in BNP, Nepal.

In Fig. 23, we observe 35 retracked PICTA data points, with 3 points excluded. These missing data points occur during months of increased WSEs. During this period, the river overflows its banks, forming smaller water bodies alongside the main river, as illustrated in Fig. 24. Consequently, the subwaveform includes multiple peaks from these smaller water bodies. The PICTA algorithm is unable to retrack the WSE from this subwaveform, resulting in the absence of data points for 3 dates during the summer months.

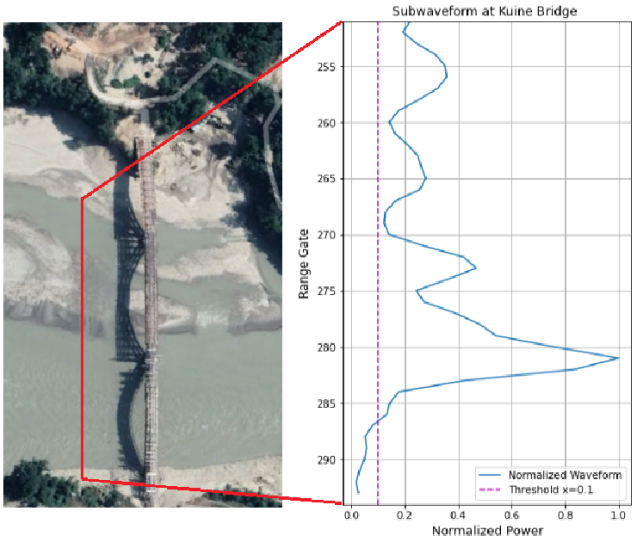

Figure 24: The left satellite image shows the Karnali River at Kuine Bridge in BNP, Nepal. The right graph presents the corresponding FF-SAR subwaveform (blue line) with the threshold at $x = 0.1$ (purple line).

Fig. 25 shows the water surface height of the Karnali River at Chisapani from 1992 to 2018. The water surface heights are referenced to an unknown local frame, resulting in a higher offset compared to the Kuine time series

than the expected 10 meters. The black line in Fig. 25 indicates a peak difference of approximately 5 meters between the highest water levels in August and the lowest in February. The PICTA derived WSEs exhibit a similar 5 m difference between August and February, with the highest peak also occurring in August. The period of increased WSEs from PICTA spans from July to September, corresponding with the long-term data from Chisapani.

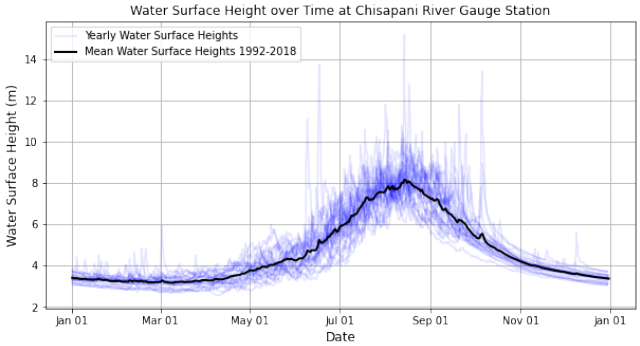

Figure 25: Time series of in-situ water surface heights relative to a local reference system at the Chisapani river gauge station from 1992–2018. The blue lines represent the continuous measurements of water surface heights for each year, while the black line indicates the averaged water surface heights over all years.

4.2 PICTA and SWOT River Water Level Profiles

Fig. 26 presents the PICTA and SWOT river water level profiles of the Karnali River segment. The PICTA and SWOT profiles exhibit very similar patterns in WSEs over the 10 km segment. Notably, both profiles have some data gaps, with the SWOT profiles exhibiting fewer gaps compared to the PICTA profiles. The gaps of the PICTA profiles will be explored further in Sec. 4.3.

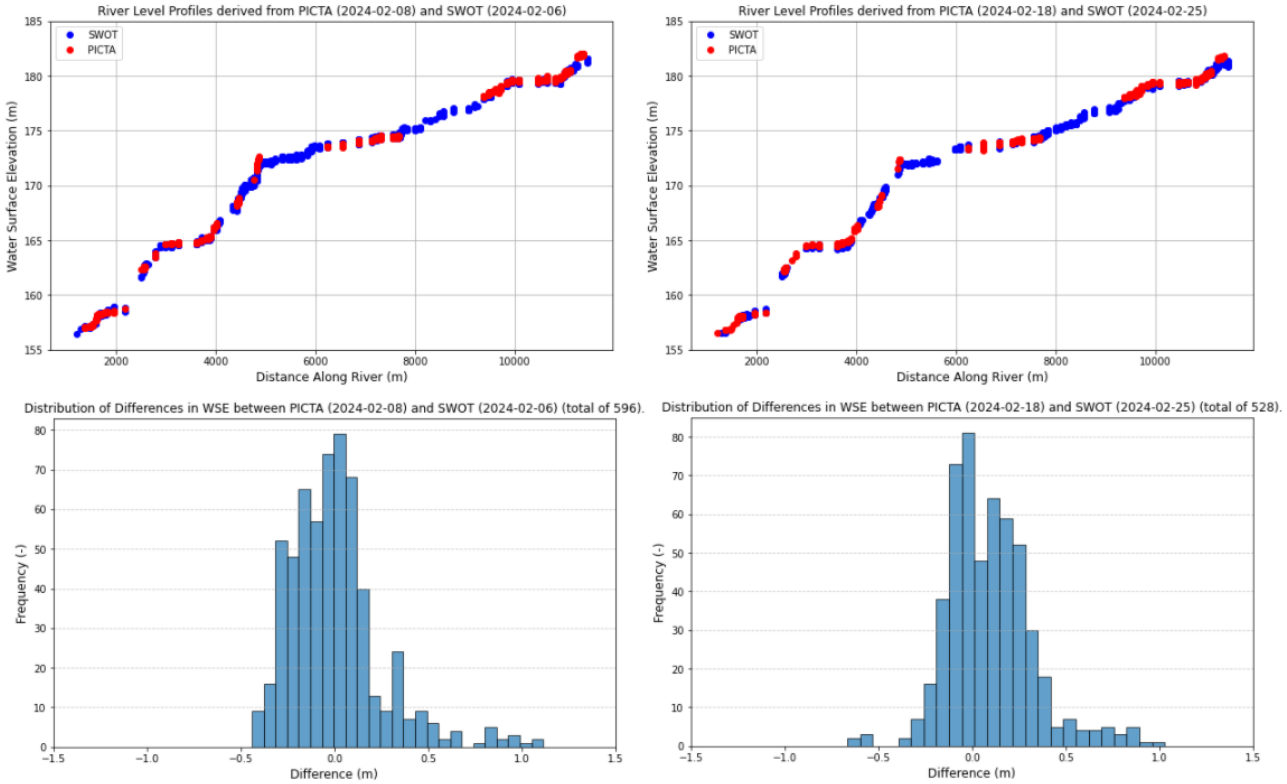

Figure 26: The graphs show the river level profiles from PICTA (red markers) and SWOT (blue markers). The WSEs are relative to WGS84. The left graph show measurement from the beginning of February whilst the right graph are obtained at the end of February, exact dates are in the title. The histograms show the differences z between the PICTA and SWOT derived WSEs for nearest neighbouring points, with a maximum allowed distance of 100 m. The measurement dates and total amount of compared points are in the titles.

The histograms in Fig. 26 present the differences between the PICTA and SWOT data points. The differences range from -0.5 m to 1.0 m for both dates. The mean and standard deviation of the differences are presented in Tab. 4, obtained using the OpenStreetMap polygon. The mean of the differences is close to zero with a standard deviation of approximately 24 cm. For the standard deviation we have to consider that according to SWOT's error budget, the precision for water surface height measurements is approximately 10 cm [3]. PICTA water level uncertainty range from 5 cm in the summer months to 20 cm in the winter months, with a mean error bound of approximately 10 cm over time, as will be detailed in Sec. 3.3.4. Additionally, we have to consider that the nearest neighbour distance reaches up to 100 m. The river slope is approximately 0.001 m/m. When comparing two points that are exactly 100 m apart along the river's track, this slope could account for an elevation difference of up to 10 cm. Taking these factors into account, the observed differences aligns with expectations.

Tab. 4 also provides the unbiased RMSE and MAD values. The unbiased RMSE values range between 0.232 m and 0.249 m. In this case the unbiased RMSE and standard deviation give similar values since the mean bias is close to zero. The scaled MAD ranges between 0.202 m and 0.208 m. These values imply a high degree of consistency between PICTA and SWOT measurements considering the uncertainties from both datasets.

To evaluate the impact of the river polygon used for the PICTA derived WSEs, the WSEs are also derived using a dynamic polygon based on the SWOT data points. The results of using a SWOT based polygon are also presented in Tab. 4. Overall, using the dynamic polygon minimally affects the unbiased RMSE and scaled MAD. As the reduction can well be within the uncertainty of the PICTA measurements. However, the use of a dynamic polygon increases the number of differences due to an increased number of PICTA data points, resulting in more overlapping pairs of PICTA and SWOT data points. This indicates that the dynamic polygon

improves the number of retracked PICTA data points, possibly by reducing the number of invalid data points excluded by the unreasonable distance criteria outlined in Eq. 7.

Profiles	**Polygon**	**Number of Differences**	**Mean Bias (m)**	**Standard Deviation (m)**	**Unbiased RMSE (m)**	**Scaled MAD (m)**
SWOT (2024-02-06) PICTA (2024-02-08)	OpenStreetMap	596	0.063	0.249	0.249	0.202
SWOT (2024-02-06) PICTA (2024-02-08)	SWOT based	601	0.021	0.245	0.245	0.188
SWOT (2024-02-25) PICTA (2024-02-18)	OpenStreetMap	528	0.093	0.250	0.232	0.208
SWOT (2024-02-25) PICTA (2024-02-18)	SWOT based	561	0.041	0.235	0.235	0.203

Table 4: Overview of metrics derived from river profiles from PICTA and SWOT. Presenting for each comparison the utilized polygon, number of differences, mean bias, standard deviation, unbiased RMSE, and scaled MAD.

4.3 River Level Profiles over Time

Fig. 27 presents the PICTA derived river level profiles for a segment of the Karnali River.

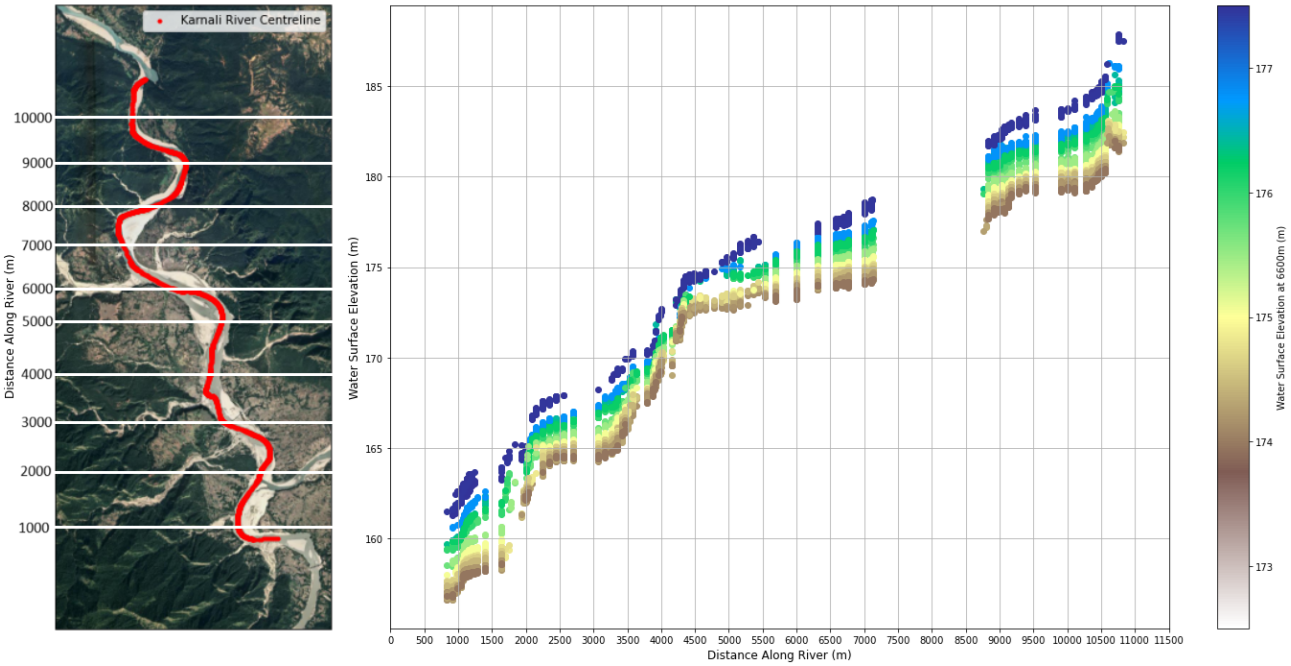

Figure 27: The left satellite image shows the segment of the Karnali River centerline. The right graph presents the PICTA river level profiles for this segment. The 38 PICTA derived profiles are acquired between 2023-02-16 and 2024-02-18. The colors are according to the WSE at chainage 6600 m along the river centerline.

We first focus on the section from 5000 m to 7000 m of the river level profiles. Fig 28 illustrates the cross-sections of the river level profiles at these locations. Between 5000 m and 7000 m along the river centerline, we observe an increase in WSE fluctuations from 2.5 m at 5000 m to 4 m at 7000 m. Notably, there are 24 data points at 5000 m, while at 7000 m, all 38 profiles have a data point. Despite the lower number of data points at 5000 m, WSE measurements are available for February and August, capturing both the highest and lowest water levels. Additionally, the mean river slope calculated over all profiles is lower at 5000 m (0.0005 m/m) compared to 7000 m (0.0015 m/m).

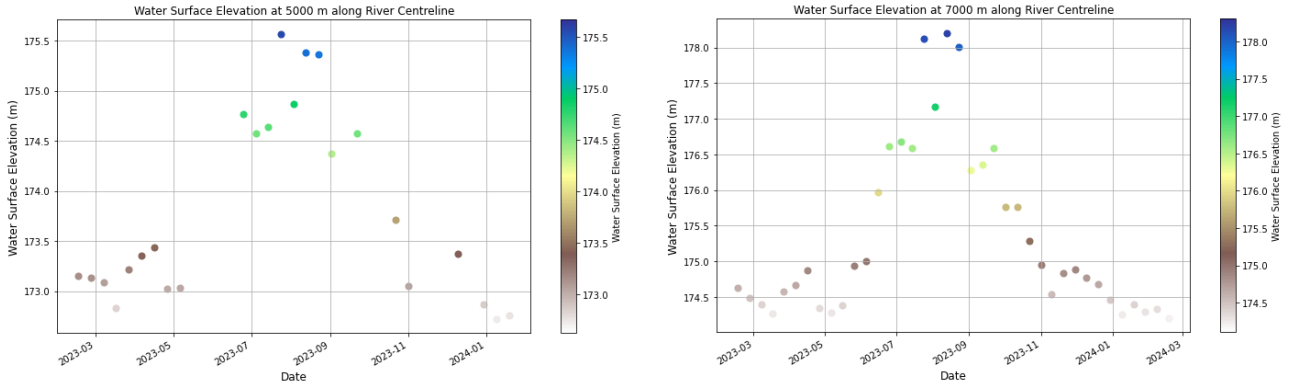

Figure 28: The left graph shows the WSE time series at 5000 m along the river centerline, containing 24 data points. The WSE fluctuation at this location is 2.5 m, ranging from the lowest water level in February to the highest water level in August. The right graph shows the WSE time series at 7000 m along the river centerline, containing all 38 data points. The WSE fluctuation at this location is 4 m.

Fig. 29 illustrates that the river can widen significantly more at 5000 m compared to 7000 m during the high-water season in the summer. Over time, the river remains narrower at 7000 m compared to 5000 m. During the summer months, when the river experiences its highest discharge (see Fig. 3), the ability of the river to widen at 5000 m prevents the WSE from rising as much as it does at the narrower section at 7000 m, where the

riverbanks cannot extend as much. Additionally, wider rivers tend to have a lower slope [21], which corresponds to the lower slope observed at 5000 m compared to 7000 m.

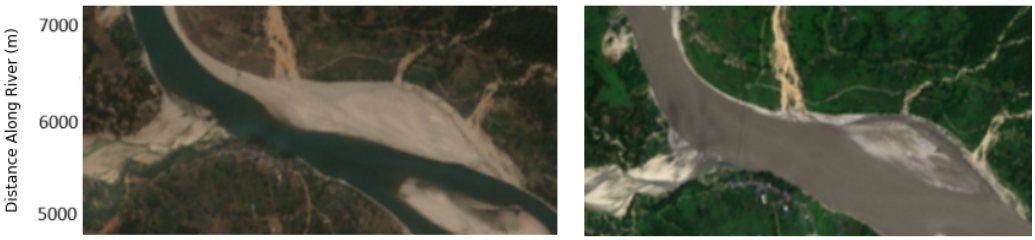

Figure 29: Satellite images depicting the geometry of a segment of the Karnali River. The left image, taken on 2023-02-22, shows the river at low water levels, while the right image, taken on 2023-08-16, shows the river at high water levels.

In Fig 27, we observe a gap in the profiles at the river bifurcation where the Karnali and Bheri rivers merge, located at 1800 m distance along river. At this location, the subwaveforms have a wider peak, leading to a higher range gate difference between the onset and decay. As a result, the retracked range gate difference $\Delta r_{retracked}$ significantly exceeds the expected river width Δr^* from the static river polygon. According to the exclusion criteria outlined in Sec. 3.2.2, these data points are flagged as invalid, leading to gaps in the river level profiles. Similarly, gaps are observed in the profiles between 6000 m and 7000 m due to tributaries from the west merging with the Karnali River.

Located at 4800 m distance along river there is a gap in the profiles, caused by small river islands that may appear seasonally depending on water levels, resulting in a multichannel river. The corresponding FF-SAR subwaveform is shown in Fig. 30. This subwaveform displays two peaks from the two river segments surrounding the island. Consequently, the onset of the first peak and the decay of the second are not fully captured in the subwaveform. As a result, the algorithm is unable to accurately identify the range gate values corresponding to the riverbanks.

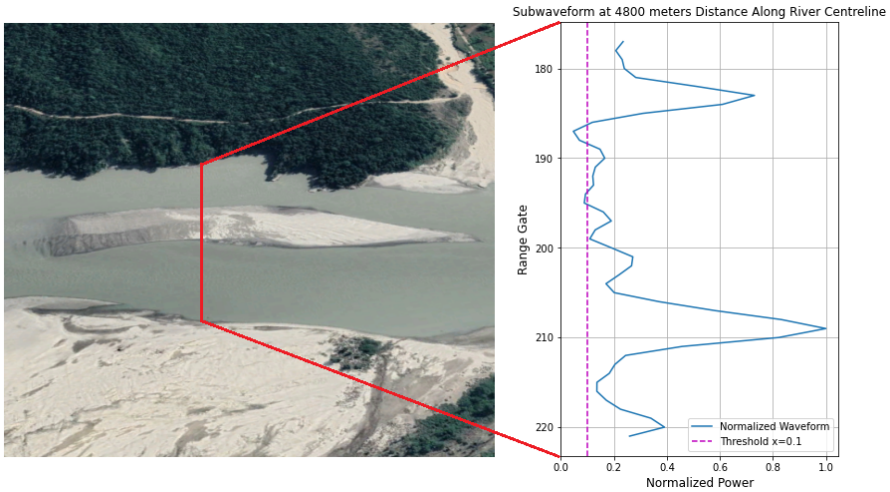

Figure 30: The left satellite image shows a river island in the Karnali river located at 4800 m along the river centreline. The right graph presents the corresponding FF-SAR subwaveform (blue line) with above the threshold at $x = 0.1$ (purple line).

The considered multichannel river is located around 4800 m along the river centerline in Fig. 27. At this location in the river level profiles, there are data points for the profiles with the highest water levels (dark blue dots), likely because the water rises above the river island. In such cases, the resulting subwaveform will only contain a single peak and the algorithm successfully retracks the range gate values for the river banks. Similarly, during the lowest water levels, the river may recede to one side of the island, also producing only one peak in the subwaveform. However, this case may result in unreasonable distances, as described in the criteria outlined in 7, due to the static river polygon not accounting for variations in river position and width. As a result, there is a significant difference between the expected river width Δr^* from the static river polygon and the retracked river width $\Delta r_{retracked}$ from PICTA at the corresponding location. This difference fails to meet the established criteria for a reasonable width. Fig. 19 illustrates the invalid data points at the location of the river island in

the FF-SAR image, located at 43000 m along track, where the range gates are flagged as invalid due to the condition of unreasonable distance. However, the waveforms at these locations could potentially be used to provide hydrological information about whether the river is single or multichannel.

Another instance of a gap in the profiles occurs around 8000 meters along the river centerline, where the Karnali River flows in a cross-track direction. Here, the onset and decay are not contained within the subwaveform. Consequently, the algorithm is unable to retrack the range gate values for the river banks. In general, the algorithm is unable to retrack the WSE for rivers located in a cross-track direction.

4.4 WSE Uncertainty over Time using a Static Polygon

Fig. 31 presents the cross-track river widths over time from PICTA, Sentinel-2, and the static river polygon from OpenStreetMap. As expected, the river width from the static river polygon $w_c^{polygon}$ is constant. The uncertainties for PICTA and Sentinel-2 are visualized by the shaded areas. The standard deviation of Sentinel-2 is assumed to be 10 meters. The standard deviation for Sentinel-2 is assumed to be 10 meters, while the standard deviation for PICTA is calculated according to Eq. 15. Both PICTA and Sentinel-2 exhibit seasonal variations, with a maximum difference of approximately 150 meters. Sentinel-2 shows a constant river width during both summer and winter intervals, while PICTA shows more variation. This discrepancy may be due to the Sentinel-2 river width being obtained at a single location, whereas PICTA averages over a 100 m section. Both PICTA and Sentinel-2 display a similar duration of increased river width from July to September, which corresponds with the WSE seasonality outlined in Sec. 4.1. The relationship between the retracked river width and WSE derived from PICTA is shown in Fig. 34 in the Appendix.

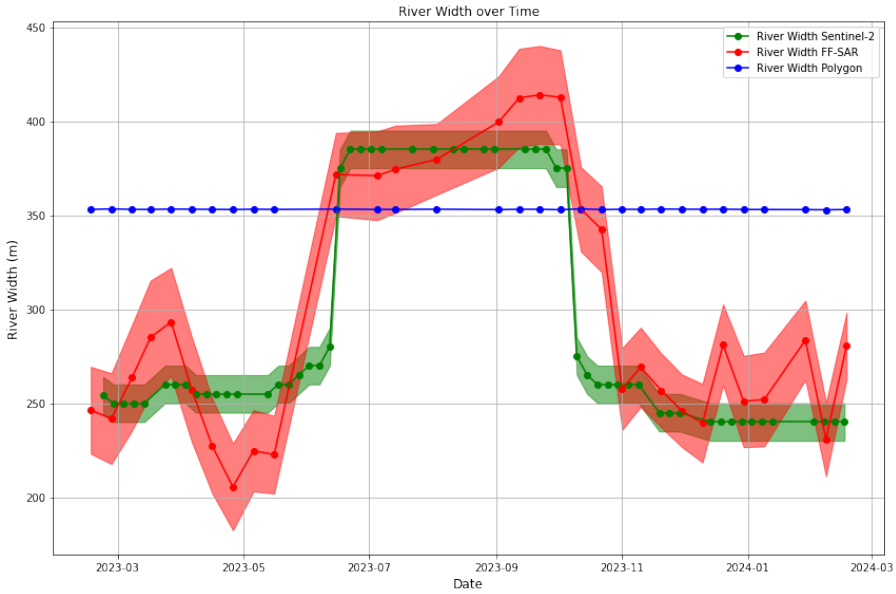

Figure 31: River widths from a 100 m section of the Karnali river over time. The green line represents the Sentinel-2 river width with a standard deviation of 10 meters, the red line represents the retracked river width from PICTA with standard deviation $\sigma_{w_c^{tracked}}$, and the blue line represents the river width from the river polygon.

The uncertainty in PICTA derived river water levels due to using a static river polygon is quantified by error bounds. These error bounds are determined by the difference between the river polygon width and the PICTA river width, following Eq. 16 and Eq. 17. Fig. 32 presents the retracked WSE with error bounds, which range from 5 cm in the summer months to 20 cm in the winter months, with a mean error bound of approximately 10 cm over time. According to Eq. 16 and Eq. 17, the difference between the PICTA river width (w_c^{PICTA}) and the static river polygon width (w_c^{polygon}) determines the WSE error bounds. This is illustrated in Fig. 31, where a smaller difference between the PICTA and river polygon widths results in smaller error bounds for the PICTA WSE in Fig. 32. This implies that the accuracy of the retracked WSE improves when the river polygon more precisely estimates the river's location. Therefore, using a dynamic river polygon could enhance the accuracy of the algorithm in retracking river water levels.

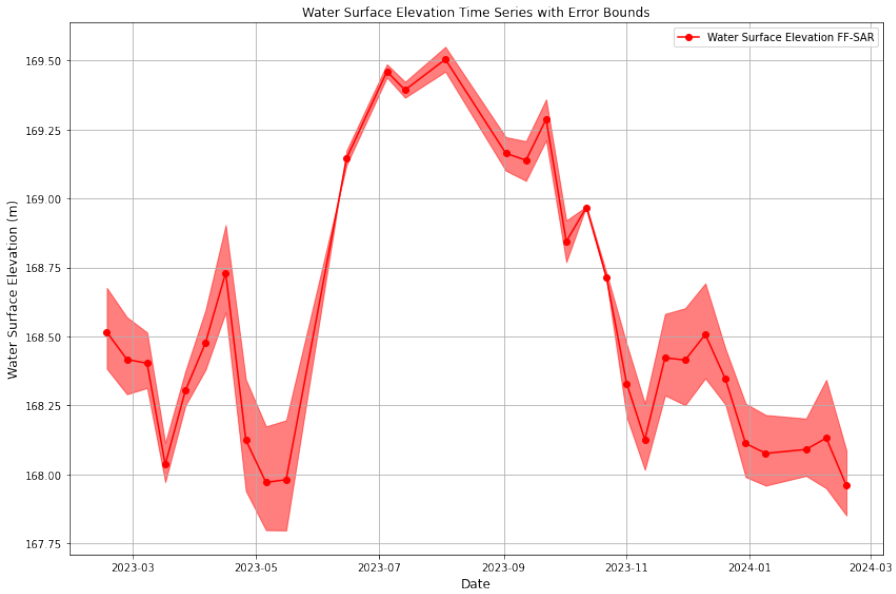

Figure 32: The retracked WSE with error bounds due to utilizing the static river polygon for a 100 meter section along the Karnali River.

5 Conclusion

This section outlines the conclusions drawn for each research question based on the results and discussion presented in Sec. 4. The first subsection evaluates the research questions, followed by a reflection on the research objectives. The second subsection provides recommendations for further research.

5.1 Insights from PICTA Derived River Level Profiles

What is the agreement between PICTA and in-situ derived water surface height time series?

The Chisapani river gauge station appeared in the waveforms between range gates 280 and 512, where no reliable WSEs could be obtained due to the RMC mode of Sentinel-6 [19]. Consequently, we compared the in-situ data from Chisapani with the PICTA data at Kuine Bridge. The analysis used the PICTA method to generate a WSE time series at Kuine Bridge, demonstrating its capability to create a WSE time series for a location along the Karnali River. The PICTA derived WSE time series at Kuine Bridge exhibited seasonal variations consistent with the expectations based on the in-situ measurements at Chisapani, showing similar peak differences and increased water levels from July to September. This alignment of seasonal trends between PICTA and in-situ data underscored the ability of the PICTA method to measure WSE over time in remote mountainous regions.

What is the agreement between PICTA and SWOT derived river level profiles?

We first generated river level profiles for PICTA and SWOT by projecting the measured WSEs onto the centerline. To assess the agreement, we compared the nearest neighboring points of both profiles. The resulting differences had a mean bias close to zero, with a standard deviation of approximately 24 cm. Considering SWOT's precision for water surface height measurements was around 10 cm [3], and PICTA water level uncertainty ranged from 5 cm in the summer months to 20 cm in the winter months, with a mean error bound of approximately 10 cm over time, we also accounted for the nearest neighbor distance reaching up to 100 m, which could result in an elevation difference of up to 10 cm. The differences between PICTA and SWOT were within the expected magnitude. Additionally, the agreement was quantified with an unbiased RMSE of approximately 24 cm, and scaled MAD values of approximately 20 cm. The comparison between river level profiles derived from SWOT and PICTA data demonstrated a high degree of consistency, despite challenges such as temporal misalignment and data gaps.

To assess the influence of using a static river polygon, we also calculated the difference between PICTA and SWOT using a dynamic SWOT-based polygon. Using dynamic river polygons based on SWOT data slightly enhanced the agreement; we observed a reduction of approximately 10 cm in the scaled MAD and an increased number of compared data points between PICTA and SWOT. These dynamic polygons better captured the river's state at the time of measurement, increasing the number of retracked PICTA data points. Overall, the PICTA and SWOT-derived WSE profiles exhibited very similar patterns, with the metrics indicating a high level of agreement between both datasets. This suggested that both could be effectively used to derive WSEs in remote mountainous regions.

How do the river level profiles vary over time?

We generated 38 PICTA river level profiles from February 2023 to February 2024, illustrating river water levels over 10-kilometer-long profiles. The WSE fluctuations and river slope along the river were related to the local river geometry. Notable gaps in the profiles provided insights into the relationship between river characteristics and the PICTA algorithm, such as the impact on river level profiles when the river transitioned from a single channel to a multichannel system. Overall, we were able to create and analyze the river level profiles over time, relating the variations to the local geometry of the river.

How does river water level uncertainty vary over time using a static river polygon?

The retracked cross-track river widths over time from PICTA demonstrated a seasonal pattern, expanding during the summer months, which aligned with observations from Sentinel-2 imagery. The static river polygon did not account for the dynamic changes of the river, resulting in discrepancies between the retracked river width and the polygon river width. Since the river bank locations from the static polygon were used in WSE calculations, this led to uncertainty. The WSE error bounds ranged from 5 cm in the summer months to 20 cm in the winter months, with a mean error bound of approximately 10 cm over time. This was in line with the bias observed in the comparison between PICTA and SWOT. The variation in retracked river width impacted the calculated WSE uncertainty, with smaller differences between the polygon width and the PICTA river width resulting in tighter error bounds. This indicated that using a dynamic river polygon would improve the accuracy of WSE measurements derived using the PICTA method.

5.2 Reflection on the Research Objectives

To assess the quality of PICTA derived river level profiles for the Karnali River in BNP.

The quality of PICTA derived river level profiles for the Karnali River has been assessed through comparisons with in-situ and SWOT derived WSE data. The comparison at Kuine Bridge demonstrated that PICTA can generate WSE time series that exhibit seasonal variations consistent with in-situ measurements. The comparison with SWOT data showed a high degree of consistency, with a mean bias close to zero and a standard deviation of approximately 24 cm, along with scaled MAD values of ∼20 cm. The use of dynamic river polygons based on SWOT further improved the agreement, reducing the scaled MAD by ∼10 cm and increasing the number of retracked PICTA data points. These results indicate that PICTA derived river level profiles exhibit very similar patterns to other measurement methods, implying that PICTA can accurately retrack WSEs in remote mountainous regions like BNP.

To assess the potential of PICTA derived river level profiles to provide insights into the hydraulic behavior of the Karnali River in BNP

The potential of PICTA-derived river level profiles to provide insights into the hydraulic behavior of rivers in BNP was assessed through the analysis of 38 profiles from February 2023 to February 2024. We generated 10-kilometer-long profiles for a section of the Karnali River, allowing us to evaluate the relationship between measured WSE fluctuations, river slope, and river width over time. We observed that both WSE fluctuations and river slope decreased at sections of the Karnali River where it could overflow its banks during high water. Notable gaps in the profiles, such as when the river transitioned from a single channel to a multichannel system, provided valuable insights into the interaction between river characteristics and the PICTA algorithm. Additionally, we assessed the WSE uncertainties when using a static river polygon for the dynamic Karnali River, suggesting that dynamic polygons could improve the accuracy of WSE measurements. Overall, PICTA's ability to capture seasonal trends and relate them to local hydraulic behavior demonstrated its significant potential for providing insights into the rivers in BNP.

5.3 Outlook

Based on the findings and challenges encountered in this study, several recommendations can be made for future research and to improve river water level retrieval utilizing PICTA.

Dynamic river polygons

The use of dynamic river polygons can improve the accuracy of PICTA derived WSE. Future research could focus on developing and integrating dynamic river polygons into the algorithm, to adjust to changes in river morphology and hydrological conditions. Sentinel-2 provides satellite imagery that could update river polygons every 5 days, though cloud coverage must be considered. Incorporating these dynamic updates will better reflect the real-time state of the river, reducing river width discrepancies and improving WSE measurement accuracy.

Multichannel Rivers

The current algorithm is unable to retrack WSE for multichannel rivers. However, the characteristic waveform of multichannel rivers could be used to detect their locations. Future research could develop methods to utilize these waveform characteristics for identifying and tracking multichannel river sections. This will provide insights into sediment transport dynamics.

Multiple River Segments and Interpolation

In this study, we primarily focused on single river segments of the Karnali River, creating 10 km long river profiles. Future studies could expand this approach to a system of interconnected rivers. The current method is unable to retrack the WSE at bifurcations. However, when WSEs are available for an interconnected river system, interpolating sections with gaps, such as bifurcations, could provide a more comprehensive understanding of the river network. Additionally, the algorithm should be optimized to automatically locate river polygons within the FF-SAR images for multiple segments. This enhancement will improve the spatial coverage and continuity of WSE measurements, resulting in more detailed profiles of a river system.

Furthermore, a future study could implement the use of height data from a Digital Elevation Model (DEM). The DEM can provide an initial estimate of the height along the river, which can be used to create a three-dimensional river polygon as input for the PICTA algorithm. This enhancement could allow for the retracking of larger river sections at once.

References

[1] The copernicus sentinel-6 mission: Enhanced continuity of satellite sea level measurements from space. *Remote Sensing of Environment*, 258:112395, 2021. ISSN 0034-4257. doi: https://doi.org/10.1016/j.rse.2021.112395. URL https://www.sciencedirect.com/science/article/pii/S0034425721001139.

[2] *Looking Beyond Nadir – Measuring river water level profiles using the Sentinel-6 altimeter and Polygon-Informed Cross-Track Altimetry (PICTA)*, July 2023.

[3] Elizabeth Altenau, Tamlin Pavelsky, Mbiawa Durand, Xiao Yang, Renato Frasson, and Liam Bendezu. The surface water and ocean topography (swot) mission river database (sword): A global river network for satellite data products. *Water Resources Research*, 57, 07 2021. doi: 10.1029/2021WR030054.

[4] Dibit Aryal, Lei Wang, Tirtha Adhikari, Jing Zhou, Xiuping Li, Maheswor Shrestha, Yuanwei Wang, and Deliang Chen. A model-based flood hazard mapping on the southern slope of himalaya. *Water*, 12:540, 02 2020. doi: 10.3390/w12020540.

[5] J. Aublanc, T. Moreau, P. Thibaut, F. Boy, F. Rémy, and N. Picot. Evaluation of sar altimetry over the antarctic ice sheet from cryosat-2 acquisitions. *Advances in Space Research*, 62(6):1307–1323, 2018. ISSN 0273-1177. doi: https://doi.org/10.1016/j.asr.2018.06.043. URL https://www.sciencedirect.com/science/article/pii/S0273117718305416. The CryoSat Satellite Altimetry Mission: Eight Years of Scientific Exploitation.

[6] Lettenmaier D.P. Pavelsky T.M. Biancamaria, S. The swot mission and its capabilities for land hydrology. 2015. doi: https://doi.org/10.1007/s10712-015-9346-y.

[7] J. Bijlmakers, J. Griffioen, and D. Karssenberg. Environmental drivers of spatio-temporal dynamics in floodplain vegetation: grasslands as habitat for megafauna in bardia national park (nepal). *Biogeosciences*, 20(6):1113–1144, 2023. doi: 10.5194/bg-20-1113-2023. URL https://bg.copernicus.org/articles/20/1113/2023/.

[8] Francois Boy, J. Cretaux, Malik Boussaroque, and Celine Tison. Improving sentinel-3 sar mode processing over lake using numerical simulations. *IEEE Transactions on Geoscience and Remote Sensing*, PP:1–1, 12 2021. doi: 10.1109/TGRS.2021.3137034.

[9] ChatGPT. https://chatgpt.com/auth/login. URL https://chatgpt.com/auth/login.

[10] Richard Coleman. Satellite altimetry and earth sciences: A handbook of techniques and applications. *Eos, Transactions American Geophysical Union*, 82:376–376, 01 2001. doi: 10.1029/01EO00233.

[11] M.K. de Jong. Water level monitoring in the karnali river, nepal, 2023. URL https://repository.tudelft.nl/islandora/object/uuid%3A1980aa85-10de-4b0b-8b8c-9382f40692ac?collection=education.

[12] DHM. https://www.dhm.gov.np/hydrology, 2024. URL https://www.dhm.gov.np/hydrology.

[13] S. Dinardo. Techniques and applications for satellite sar altimetry over water, land and ice, 2020. URL https://tuprints.ulb.tu-darmstadt.de/11343/7/Dinardo_Salvatore_Diss.pdf.

[14] Alejandro Egido and Walter Smith. Fully focused sar altimetry: Theory and applications. *IEEE Transactions on Geoscience and Remote Sensing*, PP:1–15, 01 2017. doi: 10.1109/TGRS.2016.2607122.

[15] Frithjof Ehlers, Florian Schlembach, Marcel Kleinherenbrink, and Cornelis Slobbe. Validity assessment of samosa retracking for fully-focused sar altimeter waveforms. *Advances in Space Research*, 71(3):1377–1396, 2023. ISSN 0273-1177. doi: https://doi.org/10.1016/j.asr.2022.11.034. URL https://www.sciencedirect.com/science/article/pii/S0273117722010651.

[16] E Elamir. Mean absolute deviation about median as a tool of explanatory data analysis. 1, 2012. URL https://www.iaeng.org/publication/WCE2012/WCE2012_pp324-329.pdf.

[17] eoPortal. Copernicus: Sentinel-6 michael freilich, 2016. URL https://www.eoportal.org/satellite-missions/copernicus-sentinel-6-michael-freilich#performance-specifications.

[18] eoPortal. Swot (surface water ocean topography), 2024. URL https://www.eoportal.org/satellite-missions/swot#backscattering-measurements.

[19] EUMETSAT. Sentinel-6/jason-cs alt level 1 product generation specification (l1 alt pgs) (section 7.3.13.4.3). 2021. URL https://www-cdn.eumetsat.int/files/2021-06/Sentinel-6_Jason-CS%20ALT%20Level%201%20Product%20Generation%20Specification%20%28L1%20ALT%20PGS%29_v4C_0.pdf.

[20] EUMETSAT. Sentinel-6 altimetry processing baseline, 2024. URL https://user.eumetsat.int/resources/user-guides/sentinel-6-altimetry-processing-baseline.

[21] Renato Prata de Moraes Frasson, Tamlin M. Pavelsky, Mark A. Fonstad, Michael T. Durand, George H. Allen, Guy Schumann, Christine Lion, R. Edward Beighley, and Xiao Yang. Global relationships between river width, slope, catchment area, meander wavelength, sinuosity, and discharge. *Geophysical Research Letters*, 46(6):3252–3262, 2019. doi: https://doi.org/10.1029/2019GL082027. URL https://agupubs.onlinelibrary.wiley.com/doi/abs/10.1029/2019GL082027.

[22] Lee-Lueng Fu and Anny Cazenave. *Satellite altimetry and earth sciences: a handbook of techniques and applications*. Elsevier, 2000. URL https://www.sciencedirect.com/bookseries/international-geophysics/vol/69.

[23] Ministry of Forests Goventment of Nepal and Environment. Status of tigers and prey in nepal 2022, 2022. URL https://dnpwc.gov.np/media/files/Status_of_Tigers_and_Prey_in_Nepal_2022_1.pdf.

[24] T. O. Hodson. Root-mean-square error (rmse) or mean absolute error (mae): when to use them or not. *Geoscientific Model Development*, 15(14):5481–5487, 2022. doi: 10.5194/gmd-15-5481-2022. URL https://gmd.copernicus.org/articles/15/5481/2022/.

[25] Yaron Kanza, Rajat Malik, Divesh Srivastava, Caroline Stone, and Gordon Woodhull. Data quality in data streams by modular change point detection. 2023. URL https://ceur-ws.org/Vol-3462/QDB4.pdf.

[26] Kabi Raj Khatiwada, Jeeban Panthi, Madan Lall Shrestha, and Santosh Nepal. Hydro-climatic variability in the karnali river basin of nepal himalaya. *Climate*, 4(2), 2016. ISSN 2225-1154. doi: 10.3390/cli4020017. URL https://www.mdpi.com/2225-1154/4/2/17.

[27] Donghwan Kim, Hyongki Lee, Edward Beighley, and Raphael Tshimanga. Estimating discharges for poorly gauged river basin using ensemble learning regression with satellite altimetry data and a hydrological model. 07 2021. doi: https://doi.org/10.1016/j.asr.2019.08.018.

[28] Marcel Kleinherenbrink, Marc Naeije, Cornelis Slobbe, Alejandro Egido, and Walter Smith. The performance of cryosat-2 fully-focussed sar for inland water-level estimation. *Remote Sensing of Environment*, 237:111589, 2020. ISSN 0034-4257. doi: https://doi.org/10.1016/j.rse.2019.111589. URL https://www.sciencedirect.com/science/article/pii/S0034425719306091.

[29] Michelle Kral, Mari van Lunenburg, and Jacques Alphen. The spatial distribution of ungulates and primates across the vegetation gradient in bardiya national park, west nepal. *Asian Journal of Conservation Biology*, 6:38–44, 07 2017. URL https://www.researchgate.net/publication/324692718_The_spatial_distribution_of_ungulates_and_primates_across_the_vegetation_gradient_in_Bardiya_National_Park_West_Nepal.

[30] Philippe Maillard, Nicolas Bercher, and Stéphane Calmant. New processing approaches on the retrieval of water levels in envisat and saral radar altimetry over rivers: A case study of the são francisco river, brazil. *Remote Sensing of Environment*, 156:226–241, 01 2015. doi: 10.1016/j.rse.2014.09.027.

[31] Nasa. Swot level 2 water mask raster image data product, version 2.0, 2024. URL https://podaac.jpl.nasa.gov/dataset/SWOT_L2_HR_Raster_2.0.

[32] R.K. Raney. The delay/doppler radar altimeter. *IEEE Transactions on Geoscience and Remote Sensing*, 36(5):1578–1588, 1998. doi: 10.1109/36.718861.

[33] Shirzad Roohi, Nico Sneeuw, J. Benveniste, Salvatore Dinardo, Elsayed Issawy, and Guoqing Zhang. Evaluation of cryosat-2 water level derived from different retracking scenarios over selected inland water bodies. *Advances in Space Research*, 07 2019. doi: 10.1016/j.asr.2019.06.024.

[34] V. Rosmorduc, J Benveniste, E Bronner, Salvatore Dinardo, Olivier Lauret, C Maheu, Maria Milagro-Pérez, and N Picot. *Radar Altimetry Tutorial*. 09 2011. URL https://www.researchgate.net/publication/286440946_Radar_Altimetry_Tutorial.

[35] SavetheTigers. https://savethetiger.nl/, 2023. URL https://savethetiger.nl/.

[36] Raphael Schneider, Peter Godiksen, Heidi Ranndal, Henrik Madsen, and Peter Bauer-Gottwein. Application of cryosat-2 altimetry data for river analysis and modelling. *Hydrology and Earth System Sciences*, 21:751–764, 02 2017. doi: 10.5194/hess-21-751-2017.

[37] B. Shrestha. Effects on ecosystem services value due to land use and land cover change (1990–2020) in the transboundary karnali river basin, central himalayas, 2022. URL https://link.springer.com/article/10.1007/s42452-022-05022-y#citeas.

[38] Peruri Venkataanusha, Ch Anuradha, Dr Murty, and Dr Chebrolu. Detecting outliers in high dimensional data sets using z-score methodology. *International Journal of Innovative Technology and Exploring Engineering*, 9:48–53, 11 2019. doi: 10.35940/ijitee.A3910.119119.

[39] Heidi Villadsen, Xiaoli Deng, Ole B. Andersen, Lars Stenseng, Karina Nielsen, and Per Knudsen. Improved inland water levels from sar altimetry using novel empirical and physical retrackers. *Journal of Hydrology*, 537:234–247, 2016. ISSN 0022-1694. doi: https://doi.org/10.1016/j.jhydrol.2016.03.051. URL `https://www.sciencedirect.com/science/article/pii/S0022169416301561`.

Appendix

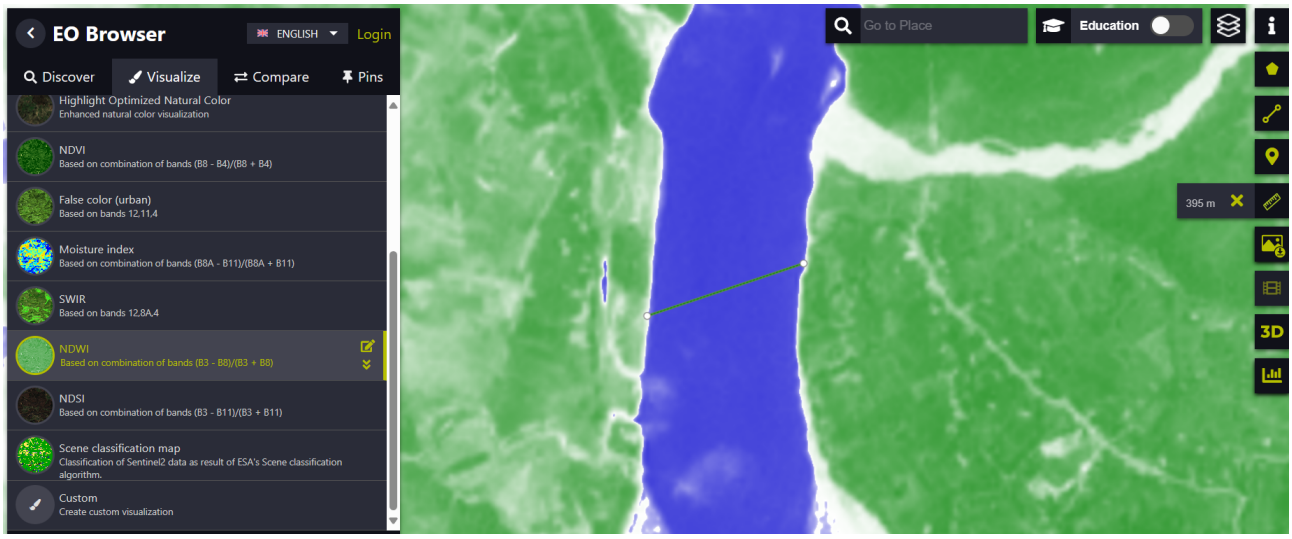

Figure 33: The EO Browser from Sentinel-Hub displaying the Normalized Water Difference Index (NWDI) used for measuring river width in the cross-track direction. This measurement is taken perpendicular to the Sentinel-6 ground track. NWDI provides river width data every 5 days, though it can be affected by cloud cover, leading to gaps in the data. The measurement uncertainty, both from the cross-track direction and the NWDI itself, has been corrected by assuming a standard deviation of 10 meters.

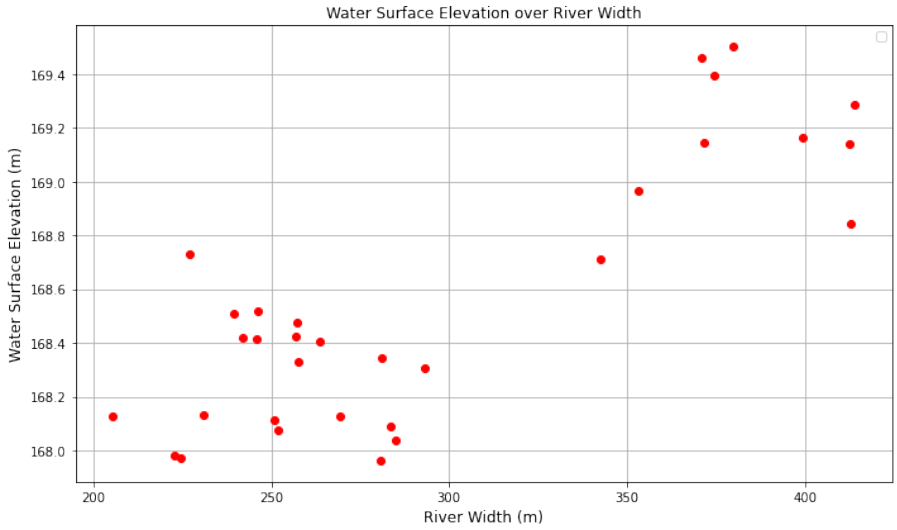

Figure 34: The relationship between the retracked WSE and the retracked river width from PICTA. The variables exhibit a strong positive correlation, with a Pearson's correlation coefficient of 0.826, based on 31 data points.